nature chemical biology

Article

https://doi.org/10.1038/s41589-024-01811-1

Transforming an ATP-dependent enzyme into a dissipative, self-assembling system

Received: 1 February 2024

Accepted: 28 November 2024

Published online: 13 January 2025

Check for updates

Yiying Li[1], Jie Zhu[1], Zhiyin Zhang[1], Jiapeng Wei[2], Fengbin Wang[3,4], Georg Meisl[2], Tuomas P. J. Knowles[2], Edward H. Egelman[3] & F. Akif Tezcan[1]

Nucleoside triphosphate (NTP)-dependent protein assemblies such as microtubules and actin filaments have inspired the development of diverse chemically fueled molecular machines and active materials but their functional sophistication has yet to be matched by design. Given this challenge, we asked whether it is possible to transform a natural adenosine 5′-triphosphate (ATP)-dependent enzyme into a dissipative self-assembling system, thereby altering the structural and functional mode in which chemical energy is used. Here we report that FtsH (filamentous temperature-sensitive protease H), a hexameric ATPase involved in membrane protein degradation, can be readily engineered to form one-dimensional helical nanotubes. FtsH nanotubes require constant energy input to maintain their integrity and degrade over time with the concomitant hydrolysis of ATP, analogous to natural NTP-dependent cytoskeletal assemblies. Yet, in contrast to natural dissipative systems, ATP hydrolysis is catalyzed by free FtsH protomers and FtsH nanotubes serve to conserve ATP, leading to transient assemblies whose lifetimes can be tuned from days to minutes through the inclusion of external ATPases in solution.

Life is characterized by a dynamic, nonequilibrium state of matter driven by constant energy flux and dissipation[1,2]. In cells, such an active state of matter is maintained primarily by nucleoside triphosphatases (NTPases) that transduce the energy stored in the phosphodiester bonds of adenosine 5′-triphosphate (ATP) and guanosine 5′-triphosphate (GTP), ultimately derived from solar photons or geothermal processes, into other chemical or mechanical forms[3–5]. NTPases can be roughly divided into two classes in terms of their overall structural and functional attributes (Fig. 1a). The first class constitutes discrete (monomeric or oligomeric) protein architectures that serve as nanoscopic machines performing a variety of NTP-driven biochemical tasks: transduction of chemical signals[6], unidirectional transport of electrons, ions or molecules[7], modification or restructuring of other cellular components[8,9] and catalysis of energetically unfavorable chemical transformations[10], among others. The second class constitutes extended, polymeric assemblies whose formation and disassembly are controlled by NTP binding and hydrolysis[11–14]. These protein assemblies, which include cytoskeletal components such as actin filaments and microtubules, constitute active materials that create motion and mechanical force through NTP-fueled polymerization and depolymerization, enabling cells to rapidly respond to spatiotemporal changes in the environment and powering processes such as cell division and motility[15–17].

Not only have the diverse functions of NTPases been widely exploited outside their natural context for developing artificial devices and materials[18–20], but NTPases have also served as inspiration for synthetic molecular systems[2,21,22]. Indeed, while early efforts in supramolecular chemistry largely targeted the design of static architectures that form and operate under equilibrium[23–25], there has been much progress in the design of artificial molecular machines[26,27], which implement

[1]Department of Chemistry and Biochemistry, University of California, San Diego, La Jolla, CA, USA. [2]Centre for Misfolding Diseases, Yusuf Hamied Department of Chemistry, University of Cambridge, Cambridge, UK. [3]Department of Biochemistry and Molecular Genetics, University of Virginia, Charlottesville, VA, USA. [4]Department of Biochemistry and Molecular Genetics, University of Alabama, Birmingham, AL, USA. e-mail: tezcan@ucsd.edu

https://doi.org/10.1038/s41589-024-01811-1

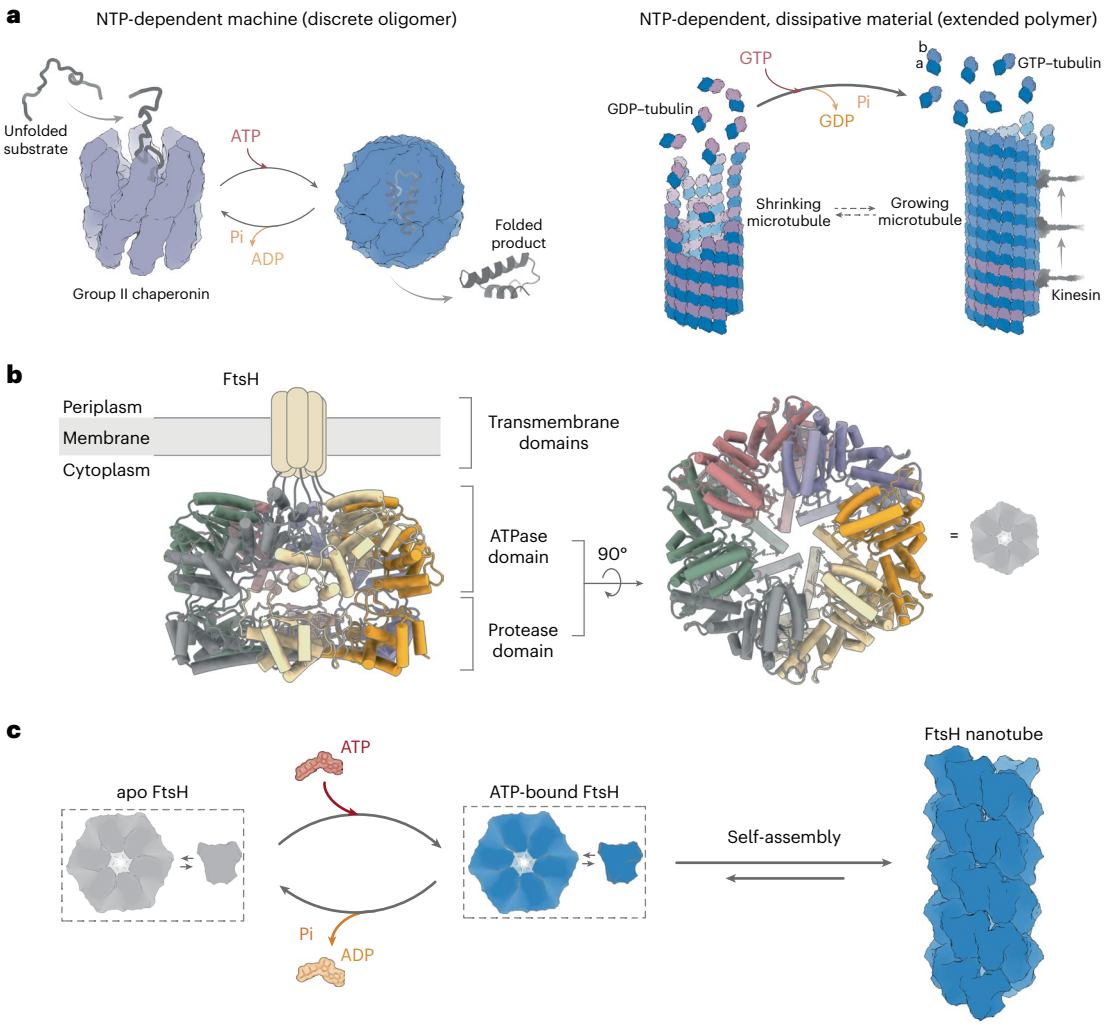

Fig. 1 | Design of FtsH assembly. a, Representative examples of natural NTPases functioning as chemical machines (left; group II chaperonin) or dissipative, self-assembling materials (right; microtubule). **b**, Structural overview of the complete FtsH in its native, membrane-anchored state (left) and its cytoplasmic domain (right). **c**, Cartoon illustration of the ATP-dependent self-assembly of FtsH.

chemically or light-driven kinetic asymmetry to power nonequilibrium structures and dynamics[28,29]. Some of these systems even directly use NTP as a chemical trigger or fuel[30–32]. Similarly, there are a growing number of synthetic self-assembling materials with dissipative properties[33–37], meaning that the formation and maintenance of their structures require continuous energy input and consumption (that is, dissipation). In turn, these assemblies can modulate the kinetics of activation and deactivation of their building blocks, thus enabling reciprocal coupling between the mechanical and the chemical states of the system and giving rise to dynamic, life-like behaviors[38–40]. A particular interest in such nonequilibrium assemblies, as opposed to systems that form under thermodynamic equilibrium, stems from the fact that they could allow quick adaptation and reconfiguration in response to changes in the environment[41]. Undoubtedly, it would also be desirable to design new proteins that match the functional sophistication of natural NTP-driven protein machines and materials. This goal would test our understanding of the design principles of natural NTPases, while also providing artificial protein platforms with new structures and functional properties not bounded by evolutionary or cellular constraints. However, despite rapid advances in the design of dynamic and stimulus-responsive protein assemblies[42–44], crafting from the bottom up a dissipative protein that can couple binding and hydrolysis of NTP (or another chemical fuel) to mechanical work or self-assembly currently remains out of reach. In light of this limitation, we considered an alternative and more readily accessible route: is it possible to transform a natural NTP-dependent enzyme into a dissipative material? In particular, we thought that it would be beneficial to generate a new NTP-dependent self-assembling system with an eye toward future uses in the design of active materials, especially given that this class of NTPases (for example, actin, tubulin and the tubulin analog FtsZ) is relatively scarce compared to the class of NTP-dependent enzymes.

Herein, we report that FtsH (filamentous temperature-sensitive protease H) (Fig. 1b), an ATPase enzyme involved in membrane protein degradation[45], can be converted into a dissipative, self-assembling platform that forms highly ordered, one-dimensional (1D) tubular structures in an ATP-dependent fashion (Fig. 1c). The conversion of the native hexameric assembly into an extended, helical architecture is accompanied by substantial conformational changes within the FtsH protomers and their interprotomer interactions. Importantly, these FtsH assemblies require the constant presence of ATP to maintain their integrity and degrade over time with the concomitant hydrolysis of ATP. The dissipative properties of FtsH assemblies are governed by an ATP-dependent equilibrium between FtsH protomers and nanotubes that dictates the kinetics of ATP hydrolysis and protein assembly or disassembly. Yet, in contrast to the natural dissipative systems such as cytoskeletal proteins, ATP hydrolysis is catalyzed exclusively by free FtsH protomers and the formation of FtsH nanotubes actually serves to conserve ATP, thereby providing an alternative mode of reciprocal

coupling between the protein assembly state and the ATP–ADP (adenosine 5′-diphosphate) chemical reaction cycle. This feature leads to transient FtsH assemblies whose lifetimes can be further modulated from days to minutes by controlling the rate of ATP consumption in the system through the addition of ATP-hydrolyzing enzymes such as hexokinase and apyrase. Our study illustrates the possibility of accessing new structural motifs and dynamic behaviors by repurposing NTPases and opens up new opportunities in the design and construction of active biomaterials.

Results

Designing ATP-dependent protein self-assembly

A consideration of actin filaments and microtubules outlines the basic requirements for a dissipative self-assembling system driven by NTP hydrolysis: (1) the building blocks (that is, protomers) bind NTP with high affinity; (2) the protomers adopt different conformational states in response to NTP binding and hydrolysis (that is, in NTP, nucleoside diphosphate (NDP) and apo states); (3) as a result of these conformational differences, self-assembly is favored by the NTP-bound protomers and not by the NDP-bound and apo states; and (4) the polymerization process induces NTP hydrolysis by the protomers, such that the assembled state can only be maintained by constant influx and consumption of NTP. From a protein design perspective, these requirements represent an increasing degree of difficulty, with requirement 1 being well within the capability of the state-of-the-art methodologies and requirement 2 being a plausible target, but requirements 3 and 4 being currently out of reach. Given this predicament, we surmised that it may be a feasible strategy to instead look for natural NTPases that, through proper re-engineering and adjustment of experimental conditions, can be converted into dissipative self-assembling systems. We considered the AAA+ (ATPases associated with diverse cellular activities) superfamily of proteins[46] to be particularly promising candidates as they already fulfill requirements 1 and 2 and have structural features that appeared conducive to the formation of 1D helical filaments in an ATP-dependent manner[47–49]. AAA+ proteins predominantly form ring-like hexameric assemblies that use ATP binding and hydrolysis to translocate and remodel various cellular substrates[5,8,50]. These processes are enabled by large ATP-induced conformational changes that necessarily involve structural flexibility of both the protomers themselves and the protomer–protomer interfaces within the hexamers[51,52]. Such flexibility within self-interacting surfaces can give rise to alternative geometries for self-assembly, as is frequently observed for actin[53,54] and tubulin[55,56] that form two-dimensional (2D) sheets under certain conditions. In fact, a large number of natively hexameric AAA+ proteins crystallize as monomers with helical crystal packing arrangements (for example, in $P6_1$ or $P6_5$ space groups)[57,58], indicating that the interprotomer interfaces in these assemblies are inherently metastable.

We specifically focused on a ubiquitous AAA+ protease found in prokaryotes and eukaryotes, namely FtsH (Fig. 1b), involved in the quality control/proteolysis of membrane-bound or cytosolic proteins[45,59,60]. FtsH[61–63] and its close homologs (for example, YME1 (ref. 51) and AFG3L2 (ref. 64)) were structurally characterized in several nucleotide-bound and substrate-bound states, revealing highly malleable interactions between the ATPase domains of the protomers. Importantly, the anchoring of FtsH to the cellular membrane through the N-terminal transmembrane (TM) domains was shown to be crucial for its ability to process membrane proteins and may also be important for stabilizing the hexameric state of FtsH[61,65,66]. Thus, we envisioned that FtsH constructs free from this constraint could potentially form nonhexameric assemblies. Following previously established protocols[61], we prepared a *Thermotoga maritima* FtsH variant devoid of the N-terminal TM domain (residues 1–146) and cysteine residues (through C255S, C513S and C564S substitutions) to avoid uncontrolled aggregation. This soluble construct, hereafter referred to as $^{\Delta C}$FtsH, was expressed in *Escherichia coli* in high yield and purified to homogeneity for further use (Supplementary Fig. 1).

ATP-dependent $^{\Delta C}$FtsH self-assembly

Analytical ultracentrifugation (AUC) measurements of $^{\Delta C}$FtsH (60 μM monomer in 100 mM NaCl) in the absence of any nucleotides revealed that it was exclusively monomeric at pH 8 and transitioned to a mixture of monomeric and dimeric species at pH 7, but existed as a mixture of monomers and hexamers at pH 6 and pH 5 (Supplementary Fig. 2). Given this pH-dependent oligomerization behavior, we next monitored the self-assembly properties of $^{\Delta C}$FtsH at different pH values (5–8) in the presence of ATP, initially using fixed $^{\Delta C}$FtsH and ATP concentrations of 75 μM and 750 μM, respectively (Fig. 2a). The protein solutions remained clear under all conditions in the absence of ATP and the corresponding negative-stain transmission electron microscopy (nsTEM) images showed discrete particles corresponding to a mixture of monomers and oligomers (Fig. 2a, top). In contrast, the addition of ATP to the $^{\Delta C}$FtsH solutions at pH 5–7 led to a visible increase in turbidity. The emergence of turbidity was immediate at pH 5 but developed over the course of several hours to days at pH 6 and 7 (Fig. 2a, bottom). In accordance with these observations, nsTEM images revealed the formation of short (200–300 nm) filamentous bundles at pH 5, a large population of single filaments with a uniform width of approximately 16 nm at pH 6, and a lower abundance of filaments mixed with hexamers at pH 7 (Fig. 2a). Dynamic light scattering (DLS) and size-exclusion chromatography (SEC) experiments further corroborated the ATP-dependent formation of large $^{\Delta C}$FtsH assemblies in solution (Fig. 2b and Supplementary Fig. 3). The high yield of $^{\Delta C}$FtsH assembly at pH 6 is ascribed to the neutralization of the overall charge of $^{\Delta C}$FtsH (estimated isoelectric point = 5.5) at this pH (Supplementary Fig. 4), which we used in all of our subsequent studies. As monitored by light scattering (λ = 340 nm) and nsTEM, the yield of ATP-dependent $^{\Delta C}$FtsH self-assembly increased upon increasing $^{\Delta C}$FtsH or ATP concentrations, consistent with an ATP-activated polymerization process (Fig. 2c,d). The initial growth stages of the $^{\Delta C}$FtsH assemblies were also captured by nsTEM measurements, which revealed that short tubular fragments formed within 1 min after mixing with ATP, followed by their evolution into micrometer-long nanotubes after 10 min (Supplementary Fig. 5).

In contrast to ATP, low-to-moderate ADP concentrations (225 μM to 1.5 mM) did not promote $^{\Delta C}$FtsH self-assembly, whereas higher ADP concentrations (≥4.5 mM) led to rapid protein precipitation (at [$^{\Delta C}$FtsH] = 75 μM) (Supplementary Fig. 6). The nsTEM images of the resulting samples showed a high population of unassembled $^{\Delta C}$FtsH oligomers and hexamers interspersed with nanotubular bundles but a limited number of isolated nanotubular structures. Similar effects were observed when $^{\Delta C}$FtsH solutions were treated with AMPPCP (phosphomethylphosphonic acid adenylate ester), a nonhydrolyzable ATP analog (Supplementary Fig. 7). These observations strongly suggest that ATP binding specifically induces an $^{\Delta C}$FtsH conformation competent for 1D self-assembly. To test this hypothesis, we prepared the ^{K207A}FtsH variant, in which the conserved K207 of the Walker A motif in $^{\Delta C}$FtsH was substituted to an alanine. The K207A substitution was previously shown to result in severely diminished ATP binding and hydrolysis activity[5,67]. Indeed, under the same self-assembly conditions as $^{\Delta C}$FtsH (75 μM ^{K207A}FtsH, large excess of ATP, pH 6.0), this variant only formed truncated fibrillar bundles in low yields even after long periods of incubation (Supplementary Fig. 8).

Consistent with an ATP-dependent activation process, the rate of $^{\Delta C}$FtsH nanotube formation increased at higher ATP concentrations (Fig. 2e). Interestingly, when these experiments were conducted at a relatively low $^{\Delta C}$FtsH concentration (30 μM) to slow down the assembly kinetics, a distinct lag phase became evident (Fig. 2e and Supplementary Fig. 9), suggestive of the formation of an activated state or a critical nucleus similar to those observed in NTP-dependent actin and tubulin polymerization (discussed below). Consistent with

https://doi.org/10.1038/s41589-024-01811-1

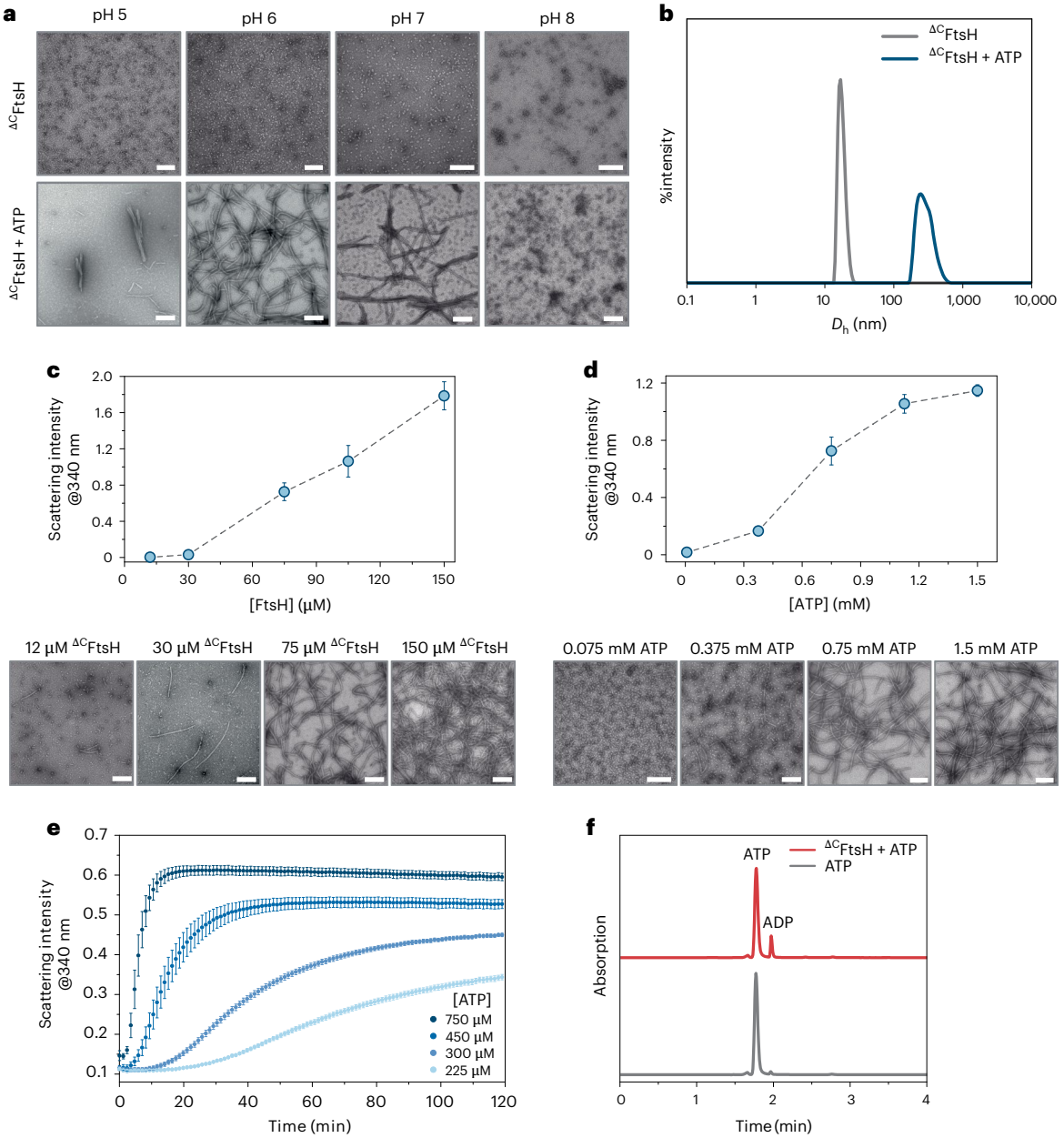

Fig. 2 | Characterization of ATP-induced $^{\Delta C}$FtsH self-assembly. a, nsTEM images of 75 μM $^{\Delta C}$FtsH incubated in the presence (bottom) and absence (top) of 750 μM ATP at different pH values. Scale bars, 200 nm. **b**, DLS profiles of $^{\Delta C}$FtsH before (gray curve) and after (blue curve) incubation with ATP. D_h refers to the hydrodynamic diameter. **c**,**d**, Dependence of light scattering intensity (at 340 nm) on $^{\Delta C}$FtsH concentration in the presence of a tenfold molar excess of ATP (**c**) or on ATP concentration at [$^{\Delta C}$FtsH] = 75 μM (**d**). Error bars represent one s.d. from the mean of three independent measurements (biological replicates). In **c**,**d**, representative nsTEM images are shown below the graphs. Scale bars, 200 nm. **e**, Dependence of $^{\Delta C}$FtsH self-assembly kinetics on ATP concentration as monitored by light scattering. [$^{\Delta C}$FtsH] = 30 μM; [ATP] = 225–750 μM; pH 6. Experimental data points and error bars reflect the mean and s.d. of three independent measurements (biological replicates). **f**, HPLC chromatograms (monitored at 260 nm) of ATP solutions incubated for 1 day in the absence (gray curve) and presence of $^{\Delta C}$FtsH (red curve, under self-assembly conditions) at pH 6 and 4 °C.

this possibility, we observed a considerable acceleration of $^{\Delta C}$FtsH nanotube assembly upon inclusion of preformed $^{\Delta C}$FtsH nanotubes (5–15% loading) as seeds in the assembly solutions (Supplementary Fig. 9). We note, however, that quantitative interpretation of turbidity in kinetic analyses is complicated by the dependence of the signal strength on both particle size and geometry. Therefore, it is also possible that the observed lag phase could arise from an ATP-dependent pre-equilibrium step for self-assembly or the time necessary for the $^{\Delta C}$FtsH nanotubes to reach a size limit below which they do not contribute to scattering.

While monitoring $^{\Delta C}$FtsH assembly kinetics, we also found through high-performance liquid chromatography (HPLC) analysis that the formation of $^{\Delta C}$FtsH nanotubes was accompanied by an increased concentration of ADP in solution above background levels (Fig. 2f). Therefore, we asked whether $^{\Delta C}$FtsH polymerizes in a dissipative manner like actin and tubulin (that is, whether the nanotube formation was coupled to ATP hydrolysis). To investigate this possibility and to understand the structural basis of ATP-dependent $^{\Delta C}$FtsH self-assembly, we set out to determine the high-resolution structure of $^{\Delta C}$FtsH nanotubes by cryogenic electron microscopy (cryo-EM).

Structural characterization of nanotubular $^{\Delta C}$FtsH assemblies

There is a considerable difference between the diameters of the $^{\Delta C}$FtsH nanotubes estimated by nsTEM (16 nm) and the FtsH hexamers determined by X-ray crystallography (12 nm)[61,62], which suggests that $^{\Delta C}$FtsH nanotubes were likely not formed through the longitudinal stacking of hexameric units. Indeed, both a close visual inspection and the 2D classification of the cryo-EM images of freshly prepared $^{\Delta C}$FtsH nanotube samples suggested a helical architecture (Fig. 3a). For high-resolution cryo-EM structure determination, we collected >9,000 micrographs and autopicked over 2 million segments through filament tracing (Supplementary Fig. 10). Approximately 75% of these segments were categorized into three groups with different symmetries by indexing their power spectra. Two of three groups yielded final volume maps through helical reconstruction at 2.5–2.6-Å resolution (Fig. 3b and Supplementary Fig. 10), providing a near-atomistic view of the nanotubular $^{\Delta C}$FtsH assembly. The two structures belonging to group 1 (C_1 symmetry, 2.6-Å resolution) and group 2 (C_2 symmetry, 2.5-Å resolution) have outer diameters of 14 and 16 nm (Supplementary Fig. 11), respectively, resulting from the slight variations in the conformations of the $^{\Delta C}$FtsH protomers and their helical packing. Importantly, in both structures, the nucleotide-binding pocket is fully occupied by an intact Mg-bound ATP molecule with a clear density for the γ-phosphate group (Fig. 3c,d), indicating that the polymerization of $^{\Delta C}$FtsH must not be coupled to ATP hydrolysis. The resolution of the structures is sufficiently high to observe the conserved interactions of the Mg-ATP moiety with the Walker A (G204, T205, G206, K207 and T208), sensor 1 (N307) and Walker B (D260 and E261) motifs (Fig. 3e). Interestingly, the arginine finger motif (R318 and R321) from the adjacent $^{\Delta C}$FtsH protomer, which is essential for conformationally gated ATP hydrolysis in the hexameric assembly, is located >10 Å away from the ATP-binding site (Fig. 3f). This observation suggests that ATP hydrolysis likely cannot take place within $^{\Delta C}$FtsH nanotubes unless there is a substantial structural perturbation to poise the Arg finger motifs in a catalytically competent position.

We next sought to understand the structural determinants of how the hexameric $^{\Delta C}$FtsH assembly is transformed into a helical architecture. The soluble, periplasmic portion of FtsH (and $^{\Delta C}$FtsH) consists of a bilobal ATPase domain (residues 147–401) and a C-terminal protease domain (414–610) connected by a flexible, 12-residue linker[59]. In the hexameric state, the two domains from each protomer associate with their counterparts from neighboring protomers to form a double-ring structure. The ring formed by the protease domains adopts an invariable, C_6-symmetric arrangement in all reported structures. The ring formed by the ATPase domains, in contrast, undergoes large-scale nucleotide state-dependent changes. These involve the tilting of the individual ATPase domains with respect to the protease domains (enabled by the flexibility of the hinge-like linker) and the resulting restructuring of their interactions with neighboring ATPase domains. In the case of the analogous YME1 protein, for which a cryo-EM structure of the active state is available, the ATPase domains form a 'spiral staircase' to couple ATP hydrolysis to the pulling of the peptide substrates into the protease ring[51].

Compared to the hexameric assembly, the $^{\Delta C}$FtsH nanotubes display substantial differences in terms of both the monomer structure and the intermonomer interactions (Fig. 3g). Firstly, as opposed to the relatively open structures of the FtsH monomers in the hexamer (observed in the full-length cryo-EM structure in the ADP-bound state), the $^{\Delta C}$FtsH monomers in the nanotubes adopt a highly compact conformation in which the ATPase domain packs tightly against the protease domain (Fig. 3h). This results in a geometry that is shaped roughly like the letter 'r' with the protease domain forming the stem and the ATPase domain the top. In this geometry, there are new interdomain interactions enabled by the unraveling of the β7 loop segment (446–459) that lies above the proteolytic Zn center. Secondly, there is an extensive restructuring of the lateral $^{\Delta C}$FtsH protomer–protomer interactions because of the translation of the protomers with respect to one another along the helical axis (Fig. 3i). As a result, the majority of the protease–protease interprotomer interactions in the hexamers are lost in the helical arrangement and partially replaced with new ones (Fig. 3i, panel 4). The ATPase domains of neighboring $^{\Delta C}$FtsH protomers retain some of the original, conserved interprotomer interactions between the α1–α2 and α8′ regions and pivot around them to accommodate the helical packing (Fig. 3i, panel 2). In addition, the restructured segment of the protease domain (446–459) is involved in new, primarily hydrophobic packing interactions with the interdomain linker of the neighboring protomer (Fig. 3i, panel 3). Lastly, there are new interfaces comprising several polar interactions between the protease and ATPase domains of adjacent protomers along the helical axis (Fig. 3i, panel 1). Consequently, each $^{\Delta C}$FtsH protomer forms interfaces with four neighboring protomers to stabilize the helical packing arrangement in contrast to two interfaces per protomer present in the hexameric assembly. In line with the observation that the $^{\Delta C}$FtsH protomers in the nanotubes are trapped in a conformational state incapable of ATP hydrolysis, we also found that $^{\Delta C}$FtsH nanotubes displayed negligible proteolytic activity compared to free $^{\Delta C}$FtsH protomers (Supplementary Fig. 12).

On the basis of our analysis of nsTEM images using FiberApp[68], we estimate the $^{\Delta C}$FtsH nanotubes to have a persistence length of ~640 nm, which is considerably shorter than those of microtubules (several millimeters) and actin filaments (~10 μm)[69]. This is indicative of looser interprotomer interactions in the $^{\Delta C}$FtsH nanotubes compared to the cytoskeletal filaments, whose interprotomer interfaces have specifically evolved for higher stiffness. Regardless, taken together with previous crystallographic and cryo-EM studies on the hexameric FtsH assemblies, our structural observations on the $^{\Delta C}$FtsH nanotubes highlight the remarkable conformational flexibility of the ATP-bound FtsH monomer and its ability to accommodate different modes of self-assembly.

Mechanism of $^{\Delta C}$FtsH self-assembly

In light of our finding that the formation of $^{\Delta C}$FtsH nanotubes is not accompanied by ATP hydrolysis, we set out to elucidate the origin of ADP generation during the self-assembly process. First, we investigated the time course of ATP consumption over timescales that are considerably longer than the formation of full-length $^{\Delta C}$FtsH nanotubes. To this end, 75 μM $^{\Delta C}$FtsH was mixed with 750 μM ATP at pH 6 to induce self-assembly within a few minutes. The HPLC analysis of the resulting mixture showed that ATP was gradually consumed over 10 days with a concomitant increase in the ADP concentration (Fig. 4a). In contrast, control samples that excluded $^{\Delta C}$FtsH from the mixture did not display any appreciable ATP hydrolysis (Supplementary Fig. 13). TEM images collected during the same time course indicated a steady population of $^{\Delta C}$FtsH nanotubes (Supplementary Fig. 14). These observations indicate that the system actively consumes ATP while maintaining the assembled state of $^{\Delta C}$FtsH. Indeed, when isolated $^{\Delta C}$FtsH nanotubes were placed in a fresh buffer solution without ATP, they disassembled within 1 h (k_{obs} = 0.1 min^{-1}) as monitored by light scattering at 340 nm, whereas those placed in an ATP-containing solution showed no evidence of dissociation (Fig. 4b and Supplementary Fig. 15).

To investigate whether $^{\Delta C}$FtsH nanotubes were capable of slow ATP hydrolysis in their assembled state, we isolated $^{\Delta C}$FtsH nanotubes that were aged for several weeks in the presence of ATP and determined their cryo-EM structures at 2.6–2.7-Å resolution (Supplementary Figs. 16 and 17). The resulting two classes of aged $^{\Delta C}$FtsH nanotubes had nearly identical helical structures to their nonaged counterparts and possessed full-occupancy Mg-ATP molecules with well-defined densities for the γ-phosphate groups (Supplementary Fig. 18). Subsequently, we prepared $^{\Delta C}$FtsH nanotubes that were internally crosslinked with EDC (1-ethyl-3-(3-dimethylaminopropyl)carbodiimide hydrochloride) and, thus, trapped in their assembled form.

https://doi.org/10.1038/s41589-024-01811-1

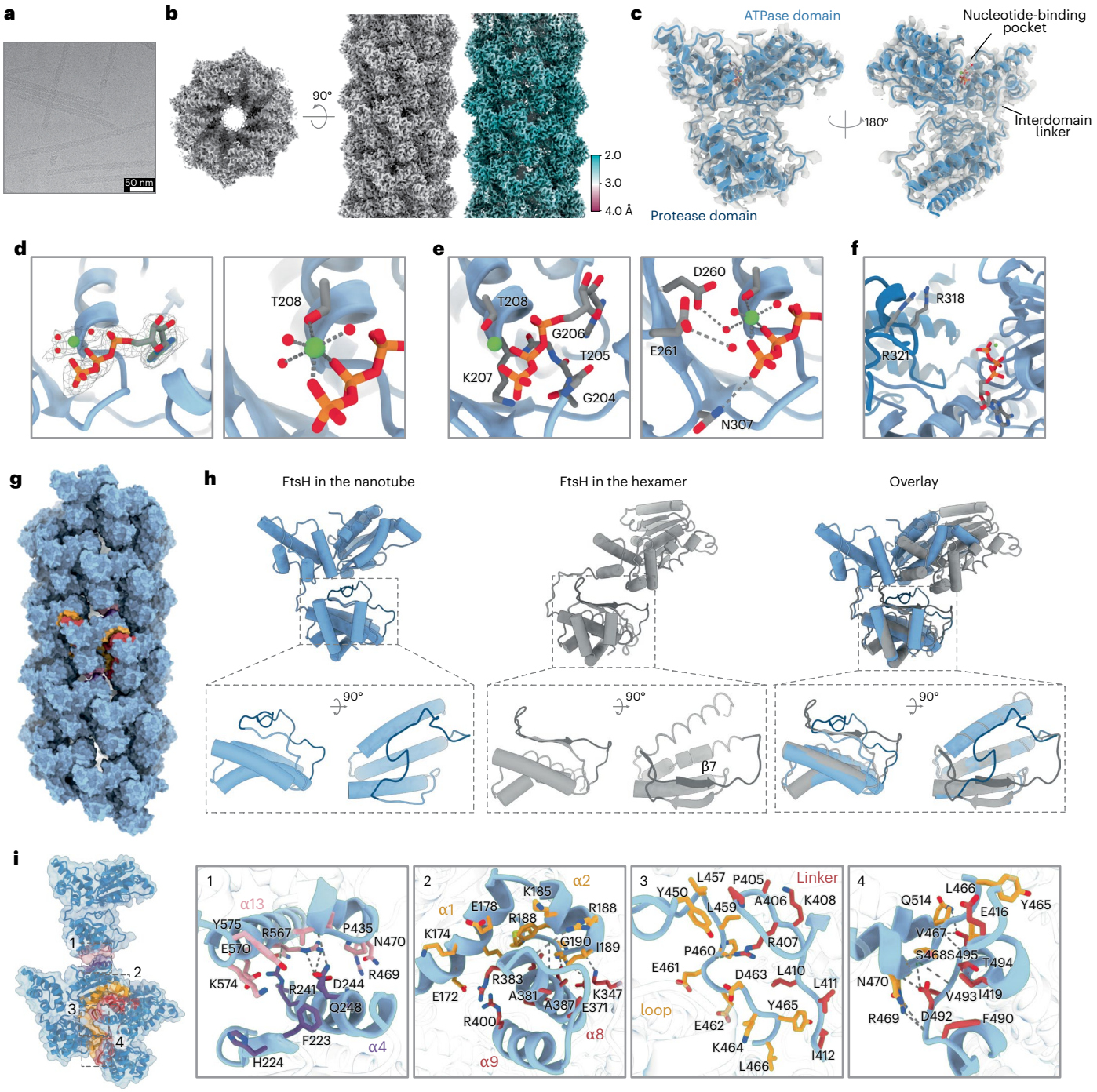

Fig. 3 | Characterization of ATP-induced $^{\Delta C}$FtsH self-assembly. a, Representative cryo-EM micrograph of $^{\Delta C}$FtsH nanotubes. Scale bar, 50 nm. **b**, Cryo-EM density map for the $^{\Delta C}$FtsH nanotube: top view (left), side view (middle) and map colored by local resolution (right). **c**, Atomic model of $^{\Delta C}$FtsH in ribbon representation showing the ATPase and protease domains. Cryo-EM density is shown as a transparent gray surface. **d**, Close-up views of the nucleotide-binding pocket (cryo-EM map shown as gray mesh at $\sigma = 3.5$), highlighting the overall Mg-ATP binding geometry (left) and Mg^{2+} coordination sphere. Mg^{2+} is shown as a green sphere and water molecules are shown as red spheres. **e**, Views of the conserved residues in the Walker A motif (G204–T208), acidic residues (D260 and E261) and sensor 1 (N307) involved in ATP binding and hydrolysis. **f**, The positioning of the arginine finger (R318 and R321) motif with respect to the ATP molecule in the neighboring $^{\Delta C}$FtsH subunit. **g**, Cryo-EM structure of the $^{\Delta C}$FtsH nanotube (group 2) in surface representation, with the buried surfaces between individual protein monomers colored in purple and pink for longitudinal interactions and colored in yellow and red for lateral interactions. **h**, Monomeric structures of $^{\Delta C}$FtsH in the nanotube (blue) and in membrane-anchored FtsH (gray, Protein Data Bank (PDB) 7TDO) and their overlay based on the protease domain. The close-up view highlights the β7 strand and its unraveling into a loop segment. **i**, Close-up views of the buried interfaces between $^{\Delta C}$FtsH monomers in the nanotubular assembly.

The crosslinked $^{\Delta C}$FtsH nanotubes displayed negligible ATP hydrolysis activity (Supplementary Fig. 19). These results, combined with the catalytically incompetent location of the Arg finger motifs within the $^{\Delta C}$FtsH nanotubes, support the conclusion that the ATP hydrolysis activity must stem from free $^{\Delta C}$FtsH monomers/hexamers that are in equilibrium with $^{\Delta C}$FtsH nanotubular assemblies. We quantified the steady-state concentration of $^{\Delta C}$FtsH monomers remaining in solution upon $^{\Delta C}$FtsH nanotube formation at increasing ATP concentrations and found that it plateaued near 1.9 μM (Supplementary Table 2 and Supplementary Fig. 22). In analogy to the literature on actin and

https://doi.org/10.1038/s41589-024-01811-1

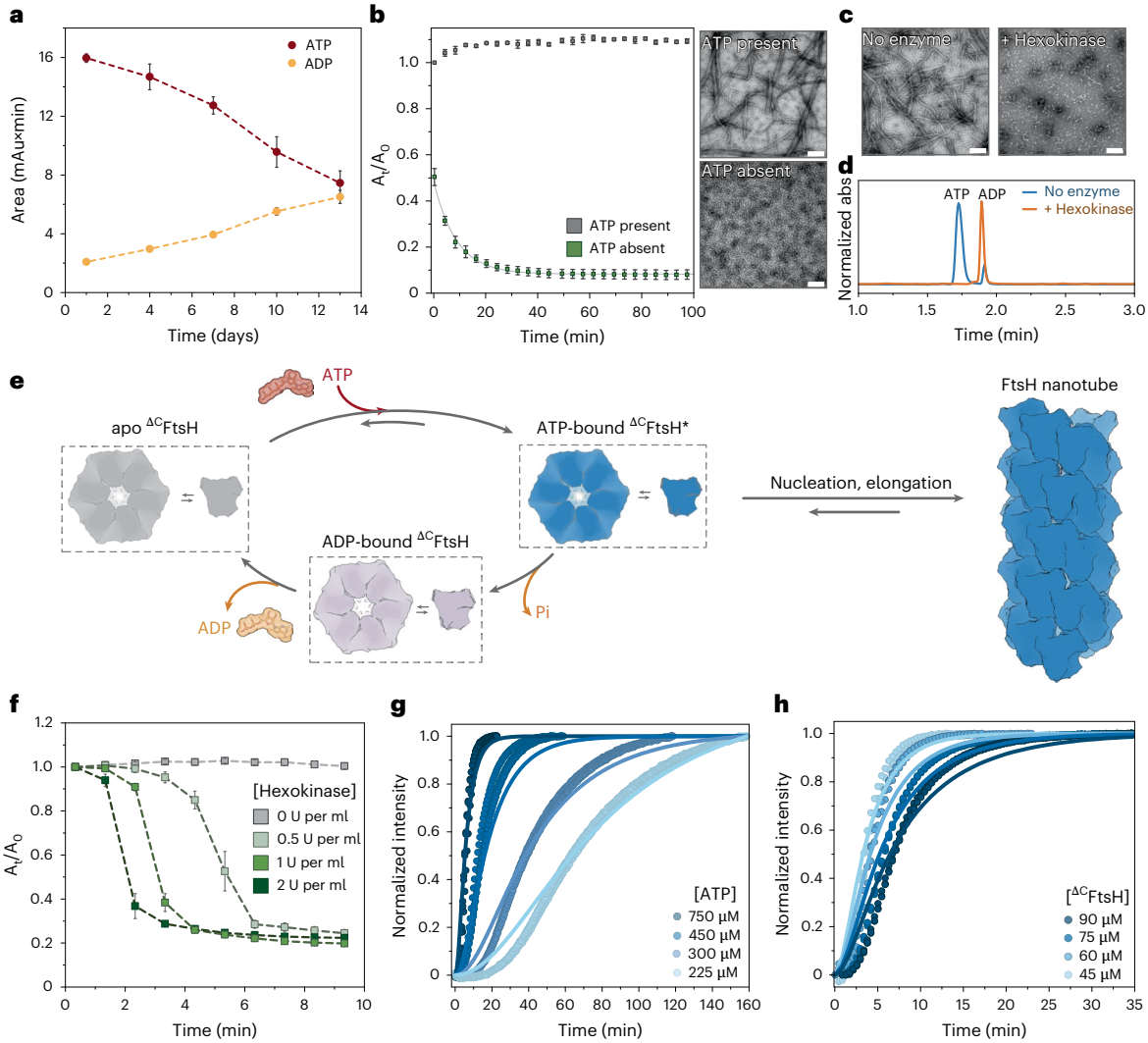

Fig. 4 | Assembly and disassembly of $^{\Delta C}$FtsH nanotubes and corresponding kinetic analysis. a, Changes in the ATP and ADP concentrations in suspensions of $^{\Delta C}$FtsH nanotubes as quantitated by HPLC over several days. Experimental data points and error bars are the mean and s.d. derived from three independent measurements. mAu, milli absorption units. **b**, Changes in light scattering intensity in suspensions of $^{\Delta C}$FtsH nanotubes following removal of ATP (green trace) or reincubation with ATP (gray trace); corresponding nsTEM images are shown on the right. Scale bars, 200 nm. The fit to monoexponential decay kinetics is shown as a solid line. Error bars represent one s.d. from the mean of three independent measurements. A_t, absorption at time t; A_0 absorption at time 0. **c**, nsTEM images of $^{\Delta C}$FtsH nanotubes before and after treatment with hexokinase. Scale bars, 200 nm. **d**, HPLC chromatograms of $^{\Delta C}$FtsH suspension before (blue curve) and after (orange curve) incubation with hexokinase for 1 h. **e**, Schematic representation of the proposed mechanism illustrating competing pathways of ATP-dependent $^{\Delta C}$FtsH self-assembly and ATP hydrolysis. **f**, Changes in light scattering after treatment of $^{\Delta C}$FtsH nanotubes with different concentrations of hexokinase. Experimental data points and error bars reflect the mean and s.d. of three independent measurements (biological replicates). **g**,**h**, Dependence of self-assembly kinetics of $^{\Delta C}$FtsH nanotubes on starting ATP concentration at 30 µM $^{\Delta C}$FtsH (**g**) or $^{\Delta C}$FtsH concentration with 750 µM ATP (**h**). Fits to the extended kinetic model are shown as solid lines.

microtubule self-assembly, we define this value as the 'critical concentration' for $^{\Delta C}$FtsH, that is, the minimal monomer concentration necessary for polymerization.

On the basis of our observations, we propose a mechanism for $^{\Delta C}$FtsH assembly in which free $^{\Delta C}$FtsH monomers are in equilibrium with their hexameric form (Fig. 4e). Upon ATP binding, the monomers adopt an activated state ($^{\Delta C}$FtsH*) competent for rapid polymerization into helical nanotubes, which are incapable of ATP hydrolysis. Yet, the same activated state can also hydrolyze ATP (in equilibrium with its hexameric form), thus undergoing autodeactivation as a competing pathway to self-assembly into nanotubes. This generates an ATP-dependent dissipative system that involves two competing protein self-assembly pathways originating from $^{\Delta C}$FtsH*: one that leads to the assembly of 'ATP-conserving' nanotubes and the other one to the assembly of 'ATP-consuming' hexamers. This bifurcation would predict a complex dependence of nanotube formation kinetics on $^{\Delta C}$FtsH concentration because both competing pathways would be favored by increasing amounts of $^{\Delta C}$FtsH. Indeed, when we raised the $^{\Delta C}$FtsH concentration from 45 to 90 µM in the presence of excess ATP (750 µM), we observed the anticipated increase in the yield of $^{\Delta C}$FtsH nanotubes but an unexpected decrease in the rate of their formation (Supplementary Fig. 20), which presumably arises from the competing formation of hexamers that hydrolyze ATP.

Given our finding that $^{\Delta C}$FtsH nanotubes and free $^{\Delta C}$FtsH monomers/hexamers exist in an equilibrium that can be modulated by the free ATP concentration, we surmised that the addition of an ATP-consuming enzyme to the system would accelerate the disassembly of the nanotubes. Indeed, the inclusion of hexokinase, an efficient

ATPase that catalyzes the phosphorylation of hexoses, in suspensions of $^{\Delta C}$FtsH nanotubes (in the presence of glucose) led to a rapid dissociation of the nanotubes within minutes (Fig. 4c,d,f). Increasing concentrations of hexokinase not only shortened the lag phase associated with the consumption of excess free ATP before the disassembly transition but also accelerated the rate of $^{\Delta C}$FtsH nanotube disassembly from 0.06 min^{-1} in the absence of enzyme to >1 min^{-1}; this upper limit was reached at 1 U per ml hexokinase and did not increase upon doubling the enzyme concentration (Fig. 4f). Because hexokinase cannot hydrolyze ATP molecules bound to $^{\Delta C}$FtsH nanotubes, we deduce that the observed disassembly kinetics must be limited by the dissociation rate constant (k_{off}) of $^{\Delta C}$FtsH monomers from the nanotubes. As each $^{\Delta C}$FtsH nanotube consists of hundreds of monomers, the observed loss of light scattering would correspond to the loss of hundreds of monomers in less than 1 min, yielding a lower estimate for k_{off} of 100 min^{-1} or 1.6 s^{-1}. Because, at equilibrium, $k_{off} = k_{on} \times [^{\Delta C}FtsH^*]_{equil.}$ and $[^{\Delta C}FtsH^*]_{equil.} \leq 1.9$ μM as previously determined, it follows that the assembly rate constant, k_{on}, must be at least 0.8×10^6 M^{-1} s^{-1}.

Next, we built a kinetic model consisting of a minimal set of differential equations and applied it to globally fit $^{\Delta C}$FtsH nanotube formation kinetics using Amylofit[70–73] (Methods). When we only included the elementary steps for (1) reversible ATP binding to $^{\Delta C}$FtsH to generate $^{\Delta C}$FtsH* and (2) simple, nucleated polymerization of $^{\Delta C}$FtsH* for the reversible formation of nanotubes, we found that the model adequately fit the ATP concentration dependence of the nanotube assembly kinetics but not the $^{\Delta C}$FtsH concentration-dependent behavior (Supplementary Figs. 21 and 22). However, when we incorporated an additional step for the $^{\Delta C}$FtsH concentration-dependent hydrolysis of ATP and fixed the monomer association and dissociation rate constants (k_{on} and k_{off}) at the experimentally determined values, all kinetics traces and trends were reproduced well, given the small set of rate parameters and the difficulty of quantitatively matching turbidity signal to aggregate mass (Fig. 4g,h and Supplementary Fig. 23). Thus, our proposed kinetic model adequately captures the mechanism of ATP-dependent, dissipative $^{\Delta C}$FtsH self-assembly.

Engineering transient $^{\Delta C}$FtsH self-assembly

An important point that emerges from these kinetic analyses is that the inherent association and dissociation dynamics of $^{\Delta C}$FtsH nanotubes are relatively fast, with the k_{on} and k_{off} values lying well within the range of those reported for actin filaments ($k_{on} = 1.3–12 \times 10^6$ M^{-1} s^{-1}, $k_{off} = 0.8–1.4$ s^{-1})[12] and microtubules ($k_{on} = 1–9 \times 10^6$ M^{-1} s^{-1}, $k_{off} = 0.1–44$ s^{-1})[74]. In comparison, the dissociation rate constants of static 1D protein assemblies such as amyloid fibrils are at least two orders of magnitude slower (for Aβ42 fibers, $k_{off} = 0.01$ s^{-1})[75]. The rapid exchange kinetics of the cytoskeletal assemblies, controlled further by their inherent NTPase activities and interactions with accessory proteins, are essential to their roles as dynamic materials that govern cellular mechanics and motility[76]. Although the mechanism of NTP dissipation in $^{\Delta C}$FtsH self-assembly is distinct from that in actin filaments and microtubules, a common feature in all cases is that the assembly-disassembly kinetics are directly coupled to ambient ATP concentrations and can rapidly respond to changes therein. Along these lines and inspired by extensive work on synthetic dissipative systems[21,22,26], we sought to identify experimental conditions to achieve transient populations of $^{\Delta C}$FtsH assemblies with controllable lifetimes (Fig. 5a). To this end, we turned to a second ATP-consuming enzyme, apyrase, which converts ATP to AMP (adenosine 5′-monophosphate) and circumvents the accumulation of ADP (as is the case with hexokinase). As described earlier, high concentrations of ADP cause $^{\Delta C}$FtsH aggregation and may interfere with ATP binding to $^{\Delta C}$FtsH.

We first showed that apyrase also could induce the rapid disassembly of $^{\Delta C}$FtsH nanotubes, with a limiting rate (>1 min^{-1} at 1 U per ml apyrase) similar to that observed with hexokinase (Fig. 5b–d). The transience of $^{\Delta C}$FtsH nanotubes requires a balance between available ATP and its rate of consumption. Upon screening various solution conditions, we observed the transient formation of $^{\Delta C}$FtsH assemblies with lifetimes on the order of tens of minutes at >300 μM ATP and 0.1–0.4 U per ml apyrase (Fig. 5e). The scattering signals increased at nearly identical rates after initiation of assembly but peaked at different time points (ranging from 35 to 10 min) with varied intensities and decay rates that scaled with enzyme concentration (Fig. 5e). nsTEM images captured during the transient cycle (0 min, 45 min and 4 h) obtained with 0.2 U per ml apyrase and 600 μM ATP confirmed that these signal changes indeed originated from assembly and disassembly of $^{\Delta C}$FtsH nanotubes (Supplementary Fig. 24). Higher ATP concentrations led to disassembly rates on the scale of several hours, whereas higher apyrase concentrations resulted in very low populations of $^{\Delta C}$FtsH assemblies caused by rapid depletion of ATP (Supplementary Fig. 25). The cyclability of this process was demonstrated by successive additions of new batches of ATP to the same sample after the system dissipated for 6–8 h (Fig. 5f). A similar behavior was observed when repeating the process with different ATP concentrations (450 or 750 μM) at constant $^{\Delta C}$FtsH (60 μM) and apyrase (0.4 U per ml) (Supplementary Fig. 26). The lifetime of $^{\Delta C}$FtsH nanotubes, defined as the time required for signal to decay to 50% of peak intensity, ranged from 19 to 30 min, again scaling (inversely) with the starting ATP concentration. The long dissipation times (≥6 h) were necessary for complete hydrolysis of ATP, full depletion of the nanotubular assemblies and improved cyclability. Shorter dissipation intervals led to gradual buildup of nanotubes during cycling (Supplementary Fig. 26). Taken together, these experiments demonstrate that the transient self-assembly of $^{\Delta C}$FtsH can be achieved by controlling the kinetics of ATP consumption.

Discussion

Here, we have described the conversion of an ATP-powered molecular machine, FtsH, into a dissipative, self-assembling system. The conversion is achieved simply by removing the membrane-anchoring domains of FtsH, which induces the structural transformation of the hexameric FtsH assemblies with cyclic symmetry into extended 1D nanotubes with helical symmetry. This transformation is enabled by the inherent structural flexibilities of the FtsH monomers and intermonomer interactions that are essential for the native function of hexameric FtsH in ATP-powered membrane protein degradation. Our findings suggest that the membrane-anchoring domains of FtsH are critical not only for localizing the enzyme at the membrane surface but also for maintaining the functional hexameric state of the enzyme as it undergoes extensive structural changes during the catalytic cycle. The facile conversion of FtsH into a fibrillar assembly also provides another example of natural proteins that lie at the brink of aggregation[77], which is perhaps an unavoidable evolutionary risk when a protein's native function requires extensive structural changes and remodeling of oligomeric interfaces that could lead to alternative modes of protein-protein interactions.

From the perspective of engineering functional materials, the $^{\Delta C}$FtsH nanotubes provide a unique system that leverages the inherent ATP-binding and ATP-hydrolyzing ability of a natural enzyme to generate a dissipative supramolecular assembly. The mechanism of energy dissipation is different from that in the cytoskeletal actin filaments and microtubules in that ATP hydrolysis is activated in the unassembled state of $^{\Delta C}$FtsH and deactivated in the assembled state. This mechanism is similar to but also distinct from previously reported synthetic ATP-dependent supramolecular systems[22,30,31], as the building block ($^{\Delta C}$FtsH) possesses native ATPase activity that renders its self-assembly inherently dissipative without requiring the presence of additional ATP-consuming enzymes. On the one hand, this mechanism precludes $^{\Delta C}$FtsH assemblies from displaying the dynamic attributes of cytoskeletal proteins (for example, rapid adaptation and motility), which are often given as a primary inspiration in the design of synthetic, nonequilibrium systems[2,21]. On the other hand, it provides an alternative mode of reciprocal coupling whereby the formation of $^{\Delta C}$FtsH

https://doi.org/10.1038/s41589-024-01811-1

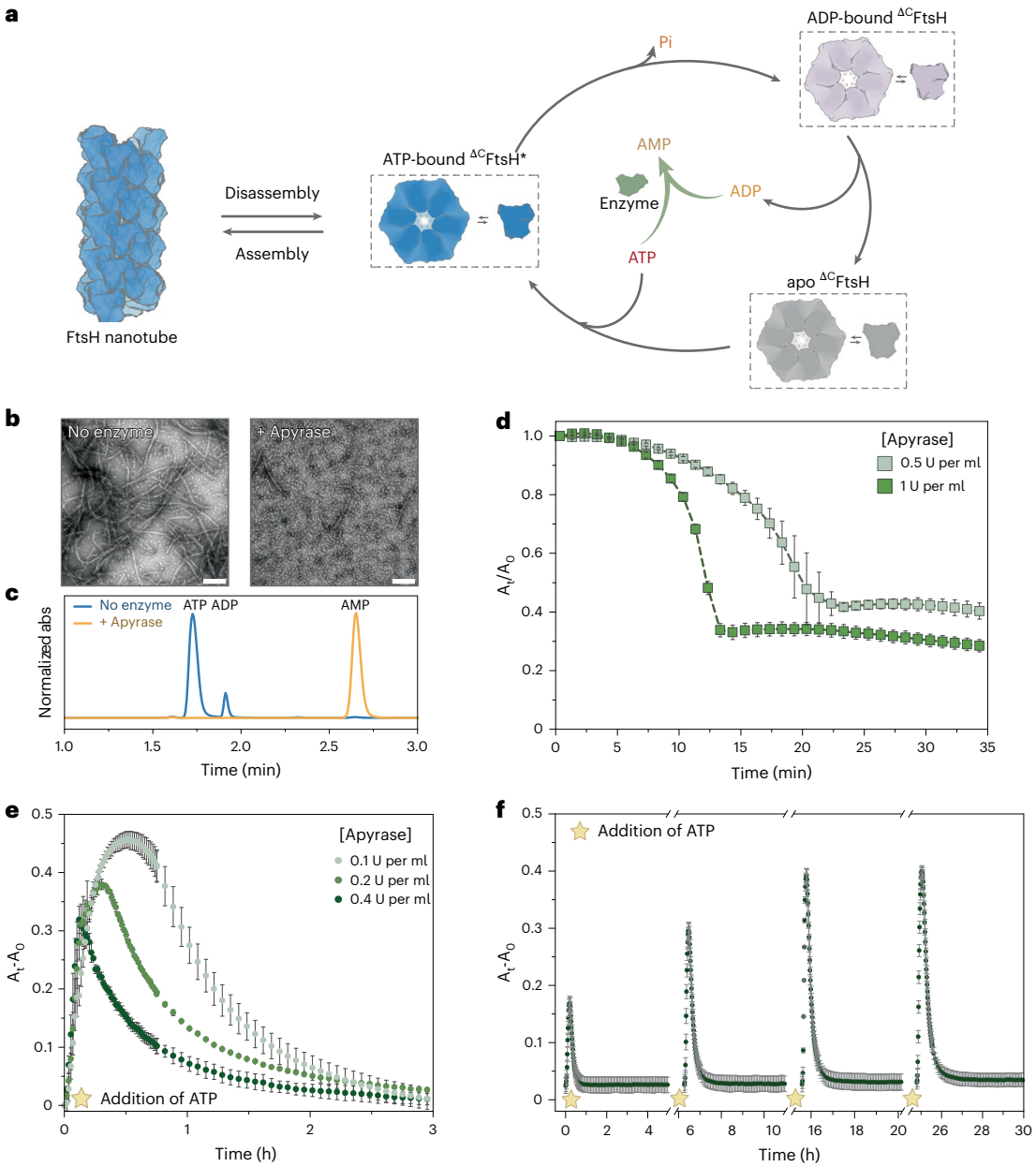

Fig. 5 | Enzyme-modulated assembly and disassembly of $^{\Delta C}$FtsH nanotubes. **a**, Schematic representation for enzyme-modulated, dissipative self-assembly of $^{\Delta C}$FtsH. **b**, nsTEM images of $^{\Delta C}$FtsH nanotubes before and after treatment with apyrase. Scale bars, 200 nm. **c**, HPLC chromatograms of suspensions of $^{\Delta C}$FtsH nanotubes before (blue curve) and after (orange curve) incubation with 1 U per ml apyrase for 1 h. **d**, Changes in scattering after treatment of $^{\Delta C}$FtsH nanotubes with different concentrations of apyrase. Experimental data points and error bars reflect the mean and s.d. determined from three independent measurements. **e**, Transient formation of $^{\Delta C}$FtsH nanotubes in solution of 600 µM ATP and 60 µM $^{\Delta C}$FtsH at different apyrase concentrations, as monitored by light scattering. Data points and error bars reflect the mean and s.d. of three independent measurements (biological replicates). **f**, Recyclable formation of transient $^{\Delta C}$FtsH assemblies upon repetitive additions of 600 µM ATP at fixed $^{\Delta C}$FtsH (60 µM) and apyrase (0.4 U per ml) concentrations, as monitored by light scattering and presented as mean and s.d. of three independent measurements (biological replicates).

assemblies exerts negative feedback on the ATP-dependent activation of the building blocks[78] and offers a different set of benefits such as the generation of stable but transient assembly states, whose lifetimes can range from days in ATP-replete conditions to tens of seconds under ATP depletion. Once such protein assembly states are coupled to different functional outcomes through proper design (for example, activation or deactivation of enzyme activity upon assembly or disassembly, cargo storage and release from the nanotube interior and interactions with cellular components), we can envision the engineering of artificial intracellular platforms whose functions can be spatiotemporally controlled through cellular ATP levels and flux. Indeed, our results show that proteolytic catalysis by $^{\Delta C}$FtsH can be turned on and off through its reversible assembly and disassembly in an ATP-dependent fashion (Supplementary Fig. 12), in analogy to natural proteins whose functions and catalytic activities are regulated by changes in their oligomerization or polymerization states in response to environmental cues and the metabolic flux inside a cell[79,80].

Online content

Any methods, additional references, Nature Portfolio reporting summaries, source data, extended data, supplementary information, acknowledgements, peer review information; details of author contributions

and competing interests; and statements of data and code availability are available at https://doi.org/10.1038/s41589-024-01811-1.

References

1. Karsenti, E. Self-organization in cell biology: a brief history. *Nat. Rev. Mol. Cell Biol.* **9**, 255–262 (2008).
2. Das, K., Gabrielli, L. & Prins, L. J. Chemically fueled self-assembly in biology and chemistry. *Angew. Chem. Int. Ed.* **60**, 20120–20143 (2021).
3. Alberts, B. The cell as a collection of protein machines: preparing the next generation of molecular biologists. *Cell* **92**, 291–294 (1998).
4. Bourne, H. R., Sanders, D. A. & Mccormick, F. The GTPase superfamily: a conserved switch for diverse cell functions. *Nature* **348**, 125–132 (1990).
5. Hanson, P. I. & Whiteheart, S. W. AAA+ proteins: have engine, will work. *Nat. Rev. Mol. Cell Biol.* **6**, 519–529 (2005).
6. Lee, M. J. & Yaffe, M. B. Protein regulation in signal transduction. *Cold Spring Harb. Perspect. Biol.* **8**, a005918 (2016).
7. Gadsby, D. C. Ion channels versus ion pumps: the principal difference, in principle. *Nat. Rev. Mol. Cell Biol.* **10**, 344–352 (2009).
8. Puchades, C., Sandate, C. R. & Lander, G. C. The molecular principles governing the activity and functional diversity of AAA+ proteins. *Nat. Rev. Mol. Cell Biol.* **21**, 43–58 (2020).
9. Zhang, J. J. et al. Mechanism of folding chamber closure in a group II chaperonin. *Nature* **463**, 379–383 (2010).
10. Ubersax, J. A. & Ferrell, J. E. Mechanisms of specificity in protein phosphorylation. *Nat. Rev. Mol. Cell Biol.* **8**, 530–541 (2007).
11. Mitchison, T. & Kirschner, M. Dynamic instability of microtubule growth. *Nature* **312**, 237–242 (1984).
12. Pollard, T. D. Actin and actin-binding proteins. *Cold Spring Harb. Perspect. Biol.* **8**, a018226 (2016).
13. Roostalu, J. & Surrey, T. Microtubule nucleation: beyond the template. *Nat. Rev. Mol. Cell Biol.* **18**, 702–710 (2017).
14. Erickson, H. P., Anderson, D. E. & Osawa, M. FtsZ in bacterial cytokinesis: cytoskeleton and force generator all in one. *Microbiol. Mol. Biol. Rev.* **74**, 504–528 (2010).
15. Akhmanova, A. & Steinmetz, M. O. Control of microtubule organization and dynamics: two ends in the limelight. *Nat. Rev. Mol. Cell Biol.* **16**, 711–726 (2015).
16. Pollard, T. D. & Cooper, J. A. Actin, a central player in cell shape and movement. *Science* **326**, 1208–1212 (2009).
17. Pollard, T. D. & Borisy, G. G. Cellular motility driven by assembly and disassembly of actin filaments. *Cell* **112**, 453–465 (2003).
18. Hoersch, D., Roh, S. H., Chiu, W. & Kortemme, T. Reprogramming an ATP-driven protein machine into a light-gated nanocage. *Nat. Nanotechnol.* **8**, 928–932 (2013).
19. Biswas, S. et al. Biomolecular robotics for chemomechanically driven guest delivery fuelled by intracellular ATP. *Nat. Chem.* **5**, 613–620 (2013).
20. Uchida, N. et al. Reconstitution of microtubule into GTP-responsive nanocapsules. *Nat. Commun.* **13**, 5424 (2022).
21. van Rossum, S. A. P., Tena-Solsona, M., van Esch, J. H., Eelkema, R. & Boekhoven, J. Dissipative out-of-equilibrium assembly of man-made supramolecular materials. *Chem. Soc. Rev.* **46**, 5519–5535 (2017).
22. Deng, J. & Walther, A. ATP-responsive and ATP-fueled self-assembling systems and materials. *Adv. Mater.* **32**, 2002629 (2020).
23. Zhu, J. et al. Protein assembly by design. *Chem. Rev.* **121**, 13701–13796 (2021).
24. Samish, I., MacDermaid, C. M., Perez-Aguilar, J. M. & Saven, J. G. Theoretical and computational protein design. *Annu. Rev. Phys. Chem.* **62**, 129–149 (2011).
25. Fleishman, S. J. & Baker, D. Role of the biomolecular energy gap in protein design, structure, and evolution. *Cell* **149**, 262–273 (2012).
26. Weissenfels, M., Gemen, J. & Klajn, R. Dissipative self-assembly: fueling with chemicals versus light. *Chem* **7**, 23–37 (2021).
27. Borsley, S., Leigh, D. A. & Roberts, B. M. W. Chemical fuels for molecular machinery. *Nat. Chem.* **14**, 728–738 (2022).
28. Ragazzon, G. & Prins, L. J. Energy consumption in chemical fuel-driven self-assembly. *Nat. Nanotechnol.* **13**, 882–889 (2018).
29. Borsley, S., Leigh, D. A. & Roberts, B. M. W. Molecular ratchets and kinetic asymmetry: giving chemistry direction. *Angew. Chem. Int. Ed.* **63**, e202400495 (2024).
30. Heinen, L. & Walther, A. Programmable dynamic steady states in ATP-driven nonequilibrium DNA systems. *Sci. Adv.* **5**, eaaw0590 (2019).
31. Maiti, S., Fortunati, I., Ferrante, C., Scrimin, P. & Prins, L. J. Dissipative self-assembly of vesicular nanoreactors. *Nat. Chem.* **8**, 725–731 (2016).
32. te Brinke, E. et al. Dissipative adaptation in driven self-assembly leading to self-dividing fibrils. *Nat. Nanotechnol.* **13**, 849–855 (2018).
33. Boekhoven, J., Hendriksen, W. E., Koper, G. J. M., Eelkema, R. & van Esch, J. H. Transient assembly of active materials fueled by a chemical reaction. *Science* **349**, 1075–1079 (2015).
34. Rizzuto, F. J. et al. A dissipative pathway for the structural evolution of DNA fibres. *Nat. Chem.* **13**, 843–849 (2021).
35. Bian, T. et al. Electrostatic co-assembly of nanoparticles with oppositely charged small molecules into static and dynamic superstructures. *Nat. Chem.* **13**, 940–949 (2021).
36. Debnath, S., Roy, S. & Ulijn, R. V. Peptide nanofibers with dynamic instability through nonequilibrium biocatalytic assembly. *J. Am. Chem. Soc.* **135**, 16789–16792 (2013).
37. Rifaie-Graham, O. et al. Photoswitchable gating of non-equilibrium enzymatic feedback in chemically communicating polymersome nanoreactors. *Nat. Chem.* **15**, 110–118 (2023).
38. Afrose, S. P., Bal, S., Chatterjee, A., Das, K. & Das, D. Designed negative feedback from transiently formed catalytic nano-structures. *Angew. Chem. Int. Ed. Engl.* **58**, 15783–15787 (2019).
39. Kriebisch, B. A. K. et al. Reciprocal coupling in chemically fueled assembly: a reaction cycle regulates self-assembly and vice versa. *J. Am. Chem. Soc.* **142**, 20837–20844 (2020).
40. Ottelé, J., Hussain, A. S., Mayer, C. & Otto, S. Chance emergence of catalytic activity and promiscuity in a self-replicator. *Nat. Catal.* **3**, 547–553 (2020).
41. Walther, A. Viewpoint: from responsive to adaptive and interactive materials and materials systems: a roadmap. *Adv. Mater.* **32**, 1905111 (2020).
42. Boyken, S. E. et al. De novo design of tunable, pH-driven conformational changes. *Science* **364**, 658–664 (2019).
43. Brodin, J. D. et al. Metal-directed, chemically tunable assembly of one-, two- and three-dimensional crystalline protein arrays. *Nat. Chem.* **4**, 375–382 (2012).
44. Yang, G. et al. Precise and reversible protein-microtubule-like structure with helicity driven by dual supramolecular interactions. *J. Am. Chem. Soc.* **138**, 1932–1937 (2016).
45. Ito, K. & Akiyama, Y. Cellular functions, mechanism of action, and regulation of FtsH protease. *Annu. Rev. Microbiol.* **59**, 211–231 (2005).
46. Neuwald, A. F., Aravind, L., Spouge, J. L. & Koonin, E. V. AAA+: a class of chaperone-like ATPases associated with the assembly, operation, and disassembly of protein complexes. *Genome Res.* **9**, 27–43 (1999).
47. Erzberger, J. P., Mott, M. L. & Berger, J. M. Structural basis for ATP-dependent DnaA assembly and replication-origin remodeling. *Nat. Struct. Mol. Biol.* **13**, 676–683 (2006).
48. Demircioglu, F. E. et al. The AAA+ ATPase TorsinA polymerizes into hollow helical tubes with 8.5 subunits per turn. *Nat. Commun.* **10**, 3262 (2019).

49. Chen, Y. J. et al. Structural polymorphism of *Methanothermobacter thermautotrophicus* MCM. *J. Mol. Biol.* **346**, 389–394 (2005).
50. Olivares, A. O., Baker, T. A. & Sauer, R. T. Mechanistic insights into bacterial AAA+ proteases and protein-remodelling machines. *Nat. Rev. Microbiol.* **14**, 33–44 (2016).
51. Puchades, C. et al. Structure of the mitochondrial inner membrane AAA+ protease YME1 gives insight into substrate processing. *Science* **358**, eaao0464 (2017).
52. Shin, M. et al. Structural basis for distinct operational modes and protease activation in AAA+ protease Lon. *Sci. Adv.* **6**, eaba8404 (2020).
53. Reynolds, M. J., Hachicho, C., Carl, A. G., Gong, R. & Alushin, G. M. Bending forces and nucleotide state jointly regulate F-actin structure. *Nature* **611**, 380–386 (2022).
54. Aebi, U., Fowler, W. E., Isenberg, G., Pollard, T. D. & Smith, P. R. Crystalline actin sheets—their structure and polymorphism. *J. Cell Biol.* **91**, 340–351 (1981).
55. Löwe, J., Li, H., Downing, K. H. & Nogales, E. Refined structure of αβ-tubulin at 3.5 Å resolution. *J. Mol. Biol.* **313**, 1045–1057 (2001).
56. Baker, T. S. & Amos, L. A. Structure of the tubulin dimer in zinc-induced sheets. *J. Mol. Biol.* **123**, 89–106 (1978).
57. Zehr, E. et al. Katanin spiral and ring structures shed light on power stroke for microtubule severing. *Nat. Struct. Mol. Biol.* **24**, 717–725 (2017).
58. Roll-Mecak, A. & Vale, R. D. Structural basis of microtubule severing by the hereditary spastic paraplegia protein spastin. *Nature* **451**, 363–367 (2008).
59. Langklotz, S., Baumann, U. & Narberhaus, F. Structure and function of the bacterial AAA protease FtsH. *Biochim. Biophys. Acta* **1823**, 40–48 (2012).
60. Asahara, Y. et al. FtsH recognizes proteins with unfolded structure and hydrolyzes the carboxyl side of hydrophobic residues. *J. Biochem.* **127**, 931–937 (2000).
61. Bieniossek, C. et al. The molecular architecture of the metallo-protease FtsH. *Proc. Natl Acad. Sci. USA* **103**, 3066–3071 (2006).
62. Bieniossek, C., Niederhauser, B. & Baumann, U. M. The crystal structure of apo-FtsH reveals domain movements necessary for substrate unfolding and translocation. *Proc. Natl Acad. Sci. USA* **106**, 21579–21584 (2009).
63. Liu, W., Schoonen, M., Wang, T., McSweeney, S. & Liu, Q. Cryo-EM structure of transmembrane AAA+ protease FtsH in the ADP state. *Commun. Biol.* **5**, 257 (2022).
64. Puchades, C. et al. Unique structural features of the mitochondrial AAA+ protease AFG3L2 reveal the molecular basis for activity in health and disease. *Mol. Cell* **75**, 1073–1085 (2019).
65. Vostrukhina, M. et al. The structure of *Aquifex aeolicus* FtsH in the ADP-bound state reveals a C_2-symmetric hexamer. *Acta Crystallogr. D* **71**, 1307–1318 (2015).
66. Shi, H., Rampello, A. J. & Glynn, S. E. Engineered AAA+ proteases reveal principles of proteolysis at the mitochondrial inner membrane. *Nat. Commun.* **7**, 13301 (2016).
67. Karata, K., Inagawa, T., Wilkinson, A. J., Tatsuta, T. & Ogura, T. Dissecting the role of a conserved motif (the second region of homology) in the AAA family of ATPases—site-directed mutagenesis of the ATP-dependent protease FtsH. *J. Biol. Chem.* **274**, 26225–26232 (1999).
68. Usov, I. & Mezzenga, R. FiberApp: an open-source software for tracking and analyzing polymers, filaments, biomacromolecules, and fibrous objects. *Macromolecules* **48**, 1269–1280 (2015).
69. Gittes, F., Mickey, B., Nettleton, J. & Howard, J. Flexural rigidity of microtubules and actin-filaments measured from thermal fluctuations in shape. *J. Cell Biol.* **120**, 923–934 (1993).
70. Meisl, G. et al. Molecular mechanisms of protein aggregation from global fitting of kinetic models. *Nat. Protoc.* **11**, 252–272 (2016).
71. Cohen, S. I. et al. Nucleated polymerization with secondary pathways. I. Time evolution of the principal moments. *J. Chem. Phys.* **135**, 065105 (2011).
72. Cohen, S. I., Vendruscolo, M., Dobson, C. M. & Knowles, T. P. Nucleated polymerization with secondary pathways. II. Determination of self-consistent solutions to growth processes described by non-linear master equations. *J. Chem. Phys.* **135**, 065106 (2011).
73. Cohen, S. I., Vendruscolo, M., Dobson, C. M. & Knowles, T. P. Nucleated polymerization with secondary pathways. III. Equilibrium behavior and oligomer populations. *J. Chem. Phys.* **135**, 065107 (2011).
74. Cleary, J. M. et al. Measurements and simulations of microtubule growth imply strong longitudinal interactions and reveal a role for GDP on the elongating end. *eLife* **11**, e75931 (2022).
75. Cohen, S. I. A. et al. Proliferation of amyloid-β42 aggregates occurs through a secondary nucleation mechanism. *Proc. Natl Acad. Sci. USA* **110**, 9758–9763 (2013).
76. Gardner, M. K. et al. Rapid microtubule self-assembly kinetics. *Cell* **146**, 582–592 (2011).
77. Garcia-Seisdedos, H., Empereur-Mot, C., Elad, N. & Levy, E. D. Proteins evolve on the edge of supramolecular self-assembly. *Nature* **548**, 244–247 (2017).
78. Schwarz, P. S., Tena-Solsona, M., Dai, K. & Boekhoven, J. Carbodiimide-fueled catalytic reaction cycles to regulate supramolecular processes. *Chem. Commun.* **58**, 1284–1297 (2022).
79. Hvorecny, K. L. & Kollman, J. M. Greater than the sum of parts: mechanisms of metabolic regulation by enzyme filaments. *Curr. Opin. Struct. Biol.* **79**, 102530 (2023).
80. Fu, J. N., Schroder, K. & Wu, H. Mechanistic insights from inflammasome structures. *Nat. Rev. Immunol.* **24**, 518–535 (2024).

Methods

Construction of $^{\Delta C}$FtsH and site-directed mutagenesis

The gene construct for the cytoplasmic domain of FtsH was obtained on the basis of a previously reported sequence (amino acids 147–610 of FtsH from *T. maritima* with K410L and K415A surface substitutions)[62], appended with an N-terminal 6xHis-tag followed by a tobacco etch virus (TEV) protease cleavage sequence (GGSENLYFQSGG)[81]. The gene construct for $^{\Delta C}$FtsH is devoid of all native cysteine residues (C255S, C513S and C564S). The ^{K207A}FtsH mutant was obtained through PCR-based site-directed mutagenesis[82], using the following DNA primers: 5′-GACAGGTGCAACACTTTTGGCACGTGCTGTCG-3′ and 5′-GTGGCACCTGTCCCGGGCGGTCC-3′.

Protein expression and purification

Bacterial expression of $^{\Delta C}$FtsH variants was performed according to previously published procedures with slight modifications[61]. Plasmids bearing the variant were transformed into BL21(DE3) *E. coli* cells and plated onto lysogeny broth (LB)–agar plates containing 100 mg L^{-1} ampicillin at 37 °C for 24 h. Isolated colonies were transferred to starter cultures (5 ml of LB medium with 100 mg L^{-1} ampicillin) and grown overnight before inoculation into 1-L LB cultures containing 100 mg L^{-1} ampicillin. After the cells were grown to an optical density of about 0.6 at 600 nm, protein expression was induced with 0.5 mM IPTG (Gold Biotechnology) for 3 h (at 37 °C shaking at 200 rpm). Cells were pelleted by centrifugation (5,000 rpm at 4 °C for 15 min), resuspended in a buffer solution containing 20 mM HEPES (pH 8), 500 mM NaCl and 5 mM β-mercaptoethanol (βME). Cell lysis was performed by sonication for 15 min on ice. Heat precipitation of *E. coli* proteins was carried out at 75 °C for 3 min. After centrifugation (13,000*g* for 20 min at 4 °C), the clarified supernatant was applied to a Ni-NTA gravity column and subjected to buffer washes containing 40 mM imidazole before elution using a gradient of imidazole (100–200 mM). Elution fractions were combined and concentrated using a 400-ml Amicon stirred cell (Millipore) and buffer-exchanged by overnight dialysis against a buffered solution containing 20 mM Tris (pH 8.0), 0.5 mM EDTA and 1 mM DTT at 4 °C. His-tag cleavage was carried out using purified TEV protease at 4 °C for 12–14 h with stirring. This solution was dialyzed against a buffer containing 20 mM HEPES (pH 8.0), 100 mM NaCl and 5 mM βME and applied to Ni-NTA. Protein without His-tag was eluted using the aforementioned buffer containing 20 mM imidazole, concentrated and buffer-exchanged into a 20 mM Tris buffer solution (pH 8) with 10 mM EDTA. Next, the protein was purified using a DuoFlow workstation station fitted with High-Q cartridge columns using a step-gradient of 0–1,000 mM NaCl. Fractions that exhibited $A_{260}/A_{280} < 1$ were pooled, concentrated and dialyzed against a buffer solution of 20 mM Tris (pH 8.0) and 100 mM NaCl. Protein purity was confirmed by SDS–PAGE and electrospray ionization mass spectrometry. The protein was then flash-frozen and kept at −80 °C until use.

Preparation of 1D $^{\Delta C}$FtsH nanotubes

Purified $^{\Delta C}$FtsH was exchanged into a buffered solution of 20 mM BisTris (pH 6.0) and 100 mM NaCl and then subjected to filtration using 0.2-µm syringe disc filter to remove aggregates. ATP, ADP, AMP and AMPPCP were dissolved in 200 mM BisTris (pH 6.0) as stock solutions and quantified by ultraviolet–visible light (UV–vis) absorption spectroscopy using the extinction coefficient ε = 15,400 M^{-1} cm^{-1} at 260 nm (ref. 83). Nucleotides were mixed with an equimolar amount of $MgCl_2$ right before adding to protein solution to ensure binding and hydrolysis by $^{\Delta C}$FtsH. In general, $^{\Delta C}$FtsH assembly was induced by mixing 75 µM $^{\Delta C}$FtsH with 750 µM ATP unless stated otherwise. The mixture was incubated at 4 °C with continuous gentle shaking. Nanotube formation resulted in increasing cloudiness of the self-assembly solutions. For different pH screening, the protein was exchanged to corresponding solutions containing 100 mM NaCl and buffered with 20 mM MES (pH 5.0), 20 mM HEPES (pH 7.0) or 20 mM Tris (pH 8.0).

nsTEM

For nsTEM sample preparation, a 3.5-µl aliquot of sample (either self-assembled $^{\Delta C}$FtsH nanotubes or proteins in solution) was applied onto freshly negatively glow-discharged carbon-coated Cu grids (Ted Pella), washed with MilliQ water, blotted using Whatman filter paper and stained using filtered 2% uranyl acetate solution before blotting again. Micrographs were collected at EM Core at the University of California, San Diego (UCSD) using a JEOL 1400 plus TEM instrument operating at 80 keV, equipped with a tungsten filament and 4,000 × 4,000 bottom-mounted Gatan One View camera. The analysis of TEM micrographs was performed in Fiji[84].

AUC

Sedimentation velocity experiments were performed to study the solution-state oligomerization behavior of $^{\Delta C}$FtsH at different pH values. First, 60 µM $^{\Delta C}$FtsH was prepared in solutions of 20 mM Tris (pH 8) and 100 mM NaCl, 20 mM Tris (pH 7) and 100 mM NaCl, 20 mM BisTris (pH 6) and 100 mM NaCl or 20 mM MES (pH 5) and 100 mM NaCl. Measurements were performed using a Beckman XL-I Analytical Ultracentrifuge (Beckman Coulter Instruments) equipped with an AN-60 Ti rotor at 41,000 rpm (131,555*g*). Data were processed using SEDFIT software with the following parameters calculated by SEDNTERP[85]: buffer density, 1.0029 g ml^{-1}; buffer viscosity, 0.01017 poise; partial specific volume, 0.7459 ml g^{-1} for $^{\Delta C}$FtsH. Theoretical sedimentation coefficients (*s*) of $^{\Delta C}$FtsH monomer were calculated as 3.4 S using HYDROPRO 10 as previously reported[86].

DLS

DLS experiments were performed using a Wyatt DynaPro NanoStar instrument. The measurements were performed using 50-µl samples to collect 15 acquisition runs of each sample with 657-nm excitation at a power setting of 100%. Averaged profiles were plotted with default settings of radius (0.5–10,000 nm).

Turbidity measurements using UV–vis spectroscopy

Nanotube formation was monitored by light scattering at 340 nm (ref. 87), using a Cary 60 UV–vis spectrometer or a Tecan Infinite M Nano+ microplate reader. For steady-state measurements, $^{\Delta C}$FtsH and ATP or ADP were mixed and incubated for 2 days at 4 °C to ensure that the growth has reached a plateau. To track growth kinetics, self-assembly was initiated by adding ATP to a $^{\Delta C}$FtsH solution prepared in buffer (20 mM BisTris (pH 6.0) and 100 mM NaCl). The measurements were started immediately after addition of ATP. Gentle shaking was applied before each reading; multiple readings from a single well were averaged. Experiments to determine the dependence of self-assembly on ATP concentration were conducted using a 30 µM $^{\Delta C}$FtsH solution in 20 mM BisTris (pH 6.0) and 100 mM NaCl. The same volume of ATP stock solution at different concentrations was added to the protein solution to reach the desired final ATP concentration (from 225 to 750 µM). Experiments to determine the dependence of self-assembly on protein concentration were performed by using different $^{\Delta C}$FtsH concentrations (from 45 to 90 µM) that were added aliquots from an ATP stock solution to achieve a final ATP concentration of 750 µM. All growth kinetics measurements were performed in triplicate. Seeds were prepared using a preformed $^{\Delta C}$FtsH nanotubes containing 75 µM $^{\Delta C}$FtsH and 750 µM ATP. The same volume of ATP stock solution with adjusted concentration was added immediately after mixing the protein solution with the seeding solution. The final concentration of $^{\Delta C}$FtsH was 30 µM and the final concentration of ATP was 225 µM.

Preparation of cryo-EM samples

Self-assembled $^{\Delta C}$FtsH nanotubes (prepared with 75 µM $^{\Delta C}$FtsH and 750 µM ATP) were incubated for 2 days at 4 °C (fresh $^{\Delta C}$FtsH assembly) or for 31 days (aged $^{\Delta C}$FtsH assembly) before grid preparation. Then, 3.5-µl aliquots of the samples were deposited onto freshly glow-discharged

holey carbon grids (EM Sciences, Grids Quantifoil Cu 2/1300 (single)) and plunged into liquid ethane after blotting using a Vitrobot Mark IV (FEI). The samples were then stored under liquid nitrogen until imaging.

Acquisition of cryo-EM data and image processing

Samples were imaged at S^2C^2 (Stanford-SLAC Cryo-EM Center) on TEM Beta (Titan Krios G3i (Thermo Fisher Scientific) equipped with a Gatan K3 direct electron detector) operating at 300 keV. Images were collected using EPU 3.5 at a magnification of ×105,000 (0.86 Å per pixel) with an electron exposure of ~50 e^- per Å^2 at a dose rate of ~1.5 e^- per frame. The objective-lens defocus range was set between −1.5 and −2.1 µm.

For the determination of the structures of 'fresh' $^{\Delta C}$FtsH nanotubes, 6,000 motion-corrected and dose-weighted micrographs were imported in cryoSPARC[88] and contrast transfer function (CTF) estimation[89] was performed. Then, 137 particles from 12 micrographs were manually picked for template generation, which was then used in the 'filament tracer' function, and 2.1 million particles were autopicked with a shift of 20 Å. The particles were then extracted with a box size of 448 pixels. Bad particles that did not contain the protein assembly segments were removed by iterative 2D classification with about 1.6 million particles remaining. Iterative 2D classification was carried out and the particles were eventually separated into 20 classes, which was further combined into three super classes (9 + 9 + 2 classes for C_1, C_2 and C_1 alternates) according to the averaged power spectra of each class. The helical symmetries of the three super classes were estimated from the calculated averaged power spectra and the actual helical symmetries were determined in cryoSPARC using the 'helical refinement' function. The helical reconstruction was further refined with nonuniform refinement enabled (an option in the 'helical refinement' function). For classes with C_1 symmetry, three-dimensional (3D) classification was carried out. The best class (one of three classes) of the helical reconstruction was selected (831,000 and 121,000 particles, respectively) for iterative rounds of helical reconstruction and CTF refinement until the resolution no longer improved. Finally, the local resolution of the resulting maps was estimated and a local filter was applied for the three volume maps. The Fourier shell correlation (FSC) estimated resolution for the maps is listed in Supplementary Table 1.

For 'aged' $^{\Delta C}$FtsH nanotubes, 11,313 motion-corrected and dose-weighted micrographs were imported into cryoSPARC and CTF estimation was performed. The template was then generated using the helical reconstruction from the ATP-induced sample mentioned above. The 'filament tracer' function was then used to autopick particles with a shift of 20 Å, resulting in 4.7 million particles. Particles were then extracted using box size of 448 pixels with 2× binning to accelerate the progress. Bad particles were removed by iterative 2D classification, resulting in ~3.8 million particles remaining. Good classes were selected to calculate the averaged power spectra, which were used as a reference to categorize into two super classes, group 1 and group 2. The helical symmetries were estimated for each super class and the actual helical symmetries were determined using the 'helical refinement' function in cryoSPARC. Particles were recentered and re-extracted unbinned for helical reconstruction. Symmetry expansion was performed on particles with C_2 symmetry. After 3D classification, 2.7 million and 1.1 million particles were accordingly selected for group 1 (C_1 symmetry) and group 2 (C_2 symmetry). After iterative rounds of helical reconstruction and CTF refinement, the local resolution of the resulting maps was estimated and a local filter was applied for the two volume maps. The FSC estimated resolution for the maps is listed in Supplementary Table 1.

Model building and refinement

A single chain of previously reported FtsH crystal structure[62] was used as an initial template and manually docked into the cryo-EM density using UCSF Chimera[90]. The structural model was subjected to iterative real-space refinement in PHENIX[91] against the cryo-EM map. The ATP molecule and tightly bound waters were identified from the clear density in the EM density map and manually built in Coot[92]. Using the refined single chain of the FtsH model, nanotube models were then generated on the basis of the determined helical symmetries. The final model was refined against the full cryo-EM map using PHENIX real-space refinement[93] and evaluated using MolProbity[94]. All molecular graphics of the resulting structures were produced using PyMOL[95] and UCSF ChimeraX.

Chromatography

All chromatography experiments were conducted using an UltiMate 3000 HPLC, equipped with UltiMate 3000 variable wavelength detectors. For analytical SEC, a 10-µl sample was injected into a single MAbPac SEC-1 (5 µm, 300 Å) analytical column (PEEK, 4.0 × 150 mm; Thermo Fisher Scientific) and monitored at 280 nm. The analysis was performed with aqueous phase (20 mM BisTris (pH 6.0) and 100 mM NaCl) at 0.3 ml min^{-1} at 25 °C. Separation and analysis of nucleotides were performed as previously reported with slight modifications[96]. Aliquots of 60–80 µl were taken from assembled samples at selected time points for reverse-phase (RP) HPLC analysis. Assemblies and protein were removed using an Amicon Ultra-0.5 30-kDa centrifugal filter (Millipore). Then, 5 µl of sample was injected into an Accucore XL C18 column (150 × 4.6 mm; Thermo Fisher Scientific) and run in the mobile phase (99% 50 mM potassium phosphate (pH 6.0) and 1% acetonitrile) at 0.8 ml min^{-1} at 25 °C. The absorbance was monitored at 260 nm. The peak area was integrated and analyzed using Chromeleon 7 software. The retention times of ATP (1.7 min) and ADP (1.9 min) were determined by injecting individual nucleotide species and the mixture of nucleotides to the column and separated under the same conditions as used for sample analyses.

Disassembly of $^{\Delta C}$FtsH nanotubes

For disassembly induced by the absence of ATP in buffer, $^{\Delta C}$FtsH nanotubes were prepared using 75 µM $^{\Delta C}$FtsH and 750 µM ATP at pH 6. Resulting suspensions of $^{\Delta C}$FtsH nanotubes were first pelleted by centrifugation at 17,000*g* for 1 min and the supernatant was discarded. The pellet was then gently resuspended in a buffer solution (20 mM BisTris (pH 6.0) and 100 mM NaCl) without ATP or a buffered solution containing 750 µM ATP as control, followed by the immediate measurement of turbidity. Then, 3.5-µl aliquots of the samples were taken to prepare TEM grids after measurements.

For enzyme-triggered disassembly, fresh preparedly $^{\Delta C}$FtsH nanotube samples containing 75 µM $^{\Delta C}$FtsH and 750 µM ATP were used. Hexokinase (Roche), glucose and apyrase (apyrase from potatoes, ATPase:ADPase ratio of ~1:1; Sigma) were prepared in stocks and frozen at −20 °C until use. Fixed volumes of hexokinase or apyrase stock were added to assembled $^{\Delta C}$FtsH samples following a gentle shaking before the measurement. Control samples were mixed with the same volume of Mill-Q water to account for the dilution of $^{\Delta C}$FtsH. Because hexokinase requires the presence of glucose to be active, 5 mM glucose was mixed with $^{\Delta C}$FtsH assemblies first in the case of hexokinase-triggered disassembly. Then, 3.5-µl aliquots of the samples were taken to prepare TEM grids after measurements. Samples used for RP-HPLC analysis were prepared by incubating 1 U per ml hexokinase (with 5 mM glucose) or apyrase with assembled $^{\Delta C}$FtsH (containing 75 µM $^{\Delta C}$FtsH and 750 µM ATP) at 20 °C for 1 h with gentle shaking. Before injecting to the C18 column, all protein content was removed by filtration of samples through a 3-kDa cutoff membrane.

Chemical crosslinking of $^{\Delta C}$FtsH nanotubes

Samples of freshly prepared $^{\Delta C}$FtsH nanotubes were incubated with 5 mM EDC and 20 mM BisTris (pH 6.0) for 10 min and then pelleted down by centrifuging at 13,800*g* for 1 min. The supernatant was removed and crosslinked nanotubes were washed multiple times with

a buffer solution (20 mM BisTris (pH 6.0) and 100 mM NaCl) until no protein or nucleotides could be detected in the supernatant by UV–vis measurements. Crosslinked nanotubes were incubated with fresh 750 μM ATP overnight before C18 HPLC analysis.

Transient assembly of $^{\Delta C}$FtsH nanotubes

For enzyme-dependent transient assembly of $^{\Delta C}$FtsH nanotubes, a solution of 60 μM $^{\Delta C}$FtsH in 20 mM BisTris (pH 6) and 100 mM NaCl was mixed with 0.1, 0.2 or 0.4 U per ml apyrase by gentle shaking. Self-assembly was then initiated by adding aliquots of ATP stock solutions to give a final ATP concentration of 600 μM, followed immediately by measurement of light scattering. TEM samples were prepared by taking 3.5-μl aliquots of samples during incubation at 45 min or after 4 h. After monitoring for 3–8 h, a fresh batch of 600 μM ATP was added to the sample to initiate the subsequent cycle. For examining the dependence of $^{\Delta C}$FtsH transient assembly cycles on ATP concentration, 60 μM $^{\Delta C}$FtsH was premixed with 0.4 U per ml apyrase in buffer. ATP stock solutions were prepared at different concentrations so that a fixed amount of volume was added to the mixed $^{\Delta C}$FtsH–apyrase solutions for the initiation of self-assembly to achieve final concentrations of 450, 600 and 750 μM. Transient assembly was monitored for 3–8 h before adding a fresh batch of ATP to initiate the next cycle.

Protein degradation assays

Protein degradation assays were carried out using a modification of an established activity assay for an FtsH analog[66]. The assays were carried out at 37 °C using 1.8 μM $^{\Delta C}$FtsH or 30 μM $^{\Delta C}$FtsH assembly in buffer containing 20 mM BisTris (pH 6.0), 100 mM NaCl, 40 μM $ZnCl_2$, 40 μM $MgCl_2$, 0.2 mg ml^{-1} β-casein and an ATP regeneration system (2 mM ATP, 20 mM 2-phosphoenolpyruvate and 18.75 U per ml pyruvate kinase). Time courses of the degradation reactions were determined by quenching aliquots from a total 100-μl reaction in SDS–PAGE loading buffer containing 2% SDS at 98 °C, with 0.2 mg ml^{-1} lysozyme supplemented as a loading control. Bands were visualized by staining with Coomassie brilliant blue R-250 (Fisher) and intensities were quantified using ImageJ and normalized to the lysozyme loading control.

Minimal model for ATP-induced self-assembly

The minimal model of ATP-induced self-assembly was developed as presented in Supplementary Fig. 21a and Supplementary Scheme 1. The model considers the following steps: (1) ATP binds the $^{\Delta C}$FtsH (apo form) to form $^{\Delta C}$FtsH* (ATP-bound monomer) and (2) $^{\Delta C}$FtsH* follows a simple nucleated polymerization mechanism to self-assemble into nanotubes. On the basis of the cryo-EM structures of $^{\Delta C}$FtsH nanotubes, we assumed that $^{\Delta C}$FtsH* is the only species that can self-assemble into nanotubes. The reversible step of nucleation was not included in the model to avoid modeling the length distribution of assembly, which would considerably complicate the model.

This resulted in the following set of differential equations:

$$\frac{dM}{dt} = 2\left(k_{on}m(t) - k_{off}\right)P(t) \quad (1)$$

$$\frac{dP}{dt} = k_n m(t)^{n_c} \quad (2)$$

$$\frac{dm}{dt} = k_a a(t)\,T(t) - k_b m(t) - 2\left(k_{on}m(t) - k_{off}\right)P(t) \quad (3)$$

$$\frac{da}{dt} = -k_a a(t)\,T(t) + k_b m(t) \quad (4)$$

$$\frac{dT}{dt} = -k_a a(t)\,T(t) + k_b m(t) \quad (5)$$

where $a(t)$ and $m(t)$ represent the $^{\Delta C}$FtsH and $^{\Delta C}$FtsH* concentrations, $T(t)$ is the concentration of ATP and $M(t)$ and $P(t)$ are the mass and number concentrations of $^{\Delta C}$FtsH nanotubes, respectively. The reversible binding of ATP to $^{\Delta C}$FtsH has k_a and k_b as the rate constants of binding and release, whereas k_n and n_c are the rate constant and reaction order of primary nucleation. k_{on} is the elongation rate constant and k_{off} is the rate constant of monomer disassociation. The numeric integration of these equations provides a simulated time evolution of $^{\Delta C}$FtsH, $^{\Delta C}$FtsH* and assembled nanotubes (Supplementary Fig. 21b). At the initial stage when only $^{\Delta C}$FtsH and ATP are present in the system, $^{\Delta C}$FtsH* forms rapidly through ATP binding $^{\Delta C}$FtsH and accumulates until nucleation takes place for self-assembly to begin. Nanotube assembly depletes $^{\Delta C}$FtsH*, leading to additional $^{\Delta C}$FtsH and ATP depletion. This model can also reproduce the disassembly of nanotubes upon ATP removal (Fig. 4b). With an initial condition of only assembled nanotubes (absence of ATP and free monomers), $^{\Delta C}$FtsH* nanotubes disassemble until a new equilibrium state is established (Supplementary Fig. 21c).

The introduction of hexokinase, which consumes ATP, leads to rapid disassembly of $^{\Delta C}$FtsH* (Fig. 4f). To model this effect, we introduce an ATP consumption term by updating equation (5) to

$$\frac{dT}{dt} = -k_a a(t)\,T(t) + k_b m(t) - k_{hyd}T(t) \quad (6)$$

where k_{hyd} denotes the rate of ATP hydrolysis. The model is only valid for the initial stage of disassembly, where only shrinkage of nanotubes occurs but not complete disassembly. ATP consumption by hexokinase is modeled as a first-order reaction to demonstrate that the minimal model can reproduce the disassembly behavior observed experimentally. The rates of ATP binding and monomer dissociation from the ends of fibrils were assumed to be fast. The numerical integration produced using the updated model, with a hydrolysis rate of $k_{hyd} = 0.1$ min^{-1} is shown in Supplementary Fig. 21d. As ATP is consumed by hexokinase, the mass of $^{\Delta C}$FtsH* nanotubes decreases and the $^{\Delta C}$FtsH concentration increases accordingly. This model is able to reproduce the observed self-assembly dependent on ATP initiation and predict the disassembly upon ATP removal either by exchange of ATP-containing buffer solution (Fig. 4b) or by introducing an efficient ATP-consuming enzyme (Fig. 4f).

Estimation of equilibrium constants

In addition to the estimation of the rate constants (discussed in 'Results'), we can obtain estimates for the equilibrium constant to provide constraints for the model. After the plateau of the $^{\Delta C}$FtsH self-assembly is reached, we assume that the reversible ATP binding to $^{\Delta C}$FtsH and the reversible association and disassociation of monomer to nanotube ends is in equilibrium.

As shown in Supplementary Scheme 1, the equilibrium of ATP binding is given as

$$k_a a_{equ} T_{equ} = k_b m_{equ} \quad (7)$$

where a_{equ}, m_{equ} and T_{equ} denote the concentrations of $^{\Delta C}$FtsH, $^{\Delta C}$FtsH* and ATP under equilibrium, respectively. If we define $k_b/k_a = K_T$, equation (7) gives

$$a_{equ} = K_T m_{equ}\frac{1}{T_{equ}} \quad (8)$$

Therefore, the total concentration of soluble protein at the plateau ($a_{equ} + m_{equ}$) can be written as a function of ATP concentration.

$$a_{equ} + m_{equ} = K_T m_{equ}\frac{1}{T_{equ}} + m_{equ} \quad (9)$$

At equilibrium, the relationship between monomer association and disassociation is given by

$$k_{on} m_{equ} P_{equ} = k_{off} P_{equ} \quad (10)$$

Therefore, the $^{\Delta C}$FtsH* concentration under equilibrium can be simply written as

$$m_{equ} = \frac{k_{off}}{k_{on}} \quad (11)$$

The total concentration of soluble FtsH ($^{\Delta C}$FtsH and $^{\Delta C}$FtsH*) at the plateau was measured experimentally by pelleting assembled nanotubes by centrifugation and determining the soluble protein concentration in the supernatant. To fit these data, we assumed that ATP was only lost to binding to $^{\Delta C}$FtsH. In reality, ATP is likely converted to ADP by hexameric $^{\Delta C}$FtsH; however, because of the excess of ATP in all measured samples, the error resulting from this approximation would pose a small effect on the ATP concentration at equilibrium. Thus, on the basis of equation (9), we used the measurement of the total protein concentration ($a_{equ} + m_{equ}$) to estimate the ATP concentration (T_{equ}) at equilibrium (Supplementary Fig. 22a). The linear fitting displays a slight deviation because at higher protein concentrations, the increased concentration of the hexameric $^{\Delta C}$FtsH in the solution leads to a higher total soluble protein concentration. However, it is still possible to estimate $K_T m_{equ}$ on the basis of the slope as ~1,000 μM, giving a good estimate for an upper bound of this quantity. Moreover, we know from these data the $m_{equ} < 1.9$ μM (Supplementary Table 2).

Scaling factor for n_c

The scaling exponent of aggregation reaction, defined as the concentration dependence of the half-time of aggregation, $t_{1/2}$, contains information about the reaction orders of nucleation process[71–73]. The relation between scaling and reaction order in a nucleated growth system is given by the power law, $t_{1/2} \propto m(0)^{-\frac{n_c}{2}}$. In our system, we can approximate $m(0) \propto [ATP]_0$, from which we get $t_{1/2} \propto T(0)^{-\frac{n_c}{2}}$. From the slope obtained by plotting half-time, $t_{1/2}$, versus the initial ATP concentration, T_0, we can get the nucleation reaction order $n_c = 3.9$ (Supplementary Fig. 22b).

Fitting of the $^{\Delta C}$FtsH assembly and disassembly kinetics using a minimal model

The data for the $^{\Delta C}$FtsH assembly kinetics at different protein or ATP concentrations were normalized and fitted using a modified local version of AmyloFit[70]. The following parameters and constraints, obtained on the basis of experimental data, were applied to the fitting: $n_c = 3.5$, $k_{off} = 100\ min^{-1}$ or $1.6\ s^{-1}$ and $K_T m_{equ} = 1{,}000$ μM. A least-squares algorithm was used to globally fit $M(t)$ obtained from the numerical integration of equation (1) across both sets of measured data. Note that the magnitude of the turbidity signal not only depends on the aggregate mass $M(t)$ but is also influenced by the size and geometry of the aggregate distribution. Therefore, these fits are treated with caution, as the model readout only approximately correlates with the measured quantity. Similarly, the values of the parameters obtained are interpreted as an order-of-magnitude guide.

As shown in Supplementary Fig. 22, the global fitting based on the minimal model can match some experimental features, especially the observed dependence of the assembly rate on ATP concentration. However, it does not predict any ATP loss by free FtsH and, thus, the long-time conversion of ATP to ADP as seen in Fig. 4a and the dependence of assembly rate on $^{\Delta C}$FtsH concentration.

Extended model for ATP-induced $^{\Delta C}$FtsH self-assembly

To account for dissipation of ATP, we included the hydrolysis of ATP as an additional step, which is dependent on the concentration of both apo FtsH and ATP-bound FtsH (Fig. 4e and Supplementary Scheme 2). This results in the addition of one term to equation (5) in the minimal model, with the involvement of both $^{\Delta C}$FtsH ($a(t)$) and $^{\Delta C}$FtsH* ($m(t)$) species in a catalytic fashion.

This results in the following set of differential equations:

$$\frac{dM}{dt} = 2\left(k_{on} m(t) - k_{off}\right) P(t) \quad (12)$$

$$\frac{dP}{dt} = k_n m(t)^{n_c} \quad (13)$$

$$\frac{dm}{dt} = k_a a(t) T(t) - k_b m(t) - 2\left(k_{on} m(t) - k_{off}\right) P(t) \quad (14)$$

$$\frac{da}{dt} = -k_a a(t) T(t) + k_b m(t) \quad (15)$$

$$\frac{dT}{dt} = -k_a a(t) T(t) + k_b m(t) - k_c a(t)^{\alpha a} m(t)^{\alpha m} T(t) \quad (16)$$

where αa and αm are the reaction orders with respect to the $^{\Delta C}$FtsH ($a(t)$) and $^{\Delta C}$FtsH* ($m(t)$) species and k_c is the rate constant for ATP-to-ADP conversion. This is a simple coarse-grained realization of a mechanism that hydrolyzes ATP, with the flexibility to depend to different degrees on the concentrations of both $^{\Delta C}$FtsH ($a(t)$) and $^{\Delta C}$FtsH* ($m(t)$). For example, if the species responsible for ATP hydrolysis is a FtsH hexamer consisting of one subunits of apo $^{\Delta C}$FtsH and five subunits of ATP-bound $^{\Delta C}$FtsH*[51], then the above equation with $\alpha a = 1$ and $\alpha m = 5$ describes the system when the FtsH hexamer is present at low concentration and in fast equilibrium with the monomeric FtsH and the rate of ATP hydrolysis is limited by the concentration of the hexamer. The time evolution of $^{\Delta C}$FtsH, $^{\Delta C}$FtsH* and self-assembled $^{\Delta C}$FtsH* nanotube mass as obtained from numerical integration of these equations is shown in Supplementary Fig. 23. During the early phase, the largest population of $^{\Delta C}$FtsH and $^{\Delta C}$FtsH* is present, leading to the substantial conversion of ATP to ADP. When most of the $^{\Delta C}$FtsH* has aggregated, the system enters into a new steady state, with pseudoequilibria for the reversible ATP binding to $^{\Delta C}$FtsH and the reversible association and disassociation of monomer to nanotube ends. The slow consumption of ATP by residual FtsH in solution leads to the gradual decrease in ATP concentration.

To evaluate how well this extended model can reproduce the experimental observations, we globally fitted the normalized data using a modified local version of AmyloFit with same constrained parameters as for fitting the minimal model (Fig. 4g,h). The values obtained from the fits are listed in Supplementary Table 3.

Statistics and reproducibility

Experiments were performed at least in duplicate to ensure reproducibility and statistical validity. Numerical data, presented as the mean ± s.d., were obtained through three biological replicates. Representative micrographs are shown from at least two independent experiments.

Reporting summary

Further information on research design is available in the Nature Portfolio Reporting Summary linked to this article.

Data availability

The principal data supporting the findings of this work are available within the figures and the Supplementary Information. The atomic coordinates and EM maps were deposited to the PDB and EM Data Bank under accession codes: PDB 8VW9 and EMD-43577 (fresh $^{\Delta C}$FtsH nanotube, group 1), 8VWA and EMD-43579 (fresh $^{\Delta C}$FtsH nanotube,

group 2), 8VWB and EMD-43580 (aged $^{\Delta C}$FtsH nanotube, group 1) and 8VWC and EMD-43581 (aged $^{\Delta C}$FtsH nanotube, group 2). Source data are provided with this paper.

References

81. Kapust, R. B., Tözsér, J., Copeland, T. D. & Waugh, D. S. The P1′ specificity of tobacco etch virus protease. *Biochem. Biophys. Res. Commun.* **294**, 949–955 (2002).
82. Liu, H. T. & Naismith, J. H. An efficient one-step site-directed deletion, insertion, single and multiple-site plasmid mutagenesis protocol. *BMC Biotechnol.* **8**, 91 (2008).
83. Menetski, J. P., Bear, D. G. & Kowalczykowski, S. C. Stable DNA heteroduplex formation catalyzed by the *Escherichia coli* Reca protein in the absence of ATP hydrolysis. *Proc. Natl Acad. Sci. USA* **87**, 21–25 (1990).
84. Schindelin, J. et al. Fiji: an open-source platform for biological-image analysis. *Nat. Methods* **9**, 676–682 (2012).
85. Philo, J. S. SEDNTERP: a calculation and database utility to aid interpretation of analytical ultracentrifugation and light scattering data. *Eur. Biophys. J.* **52**, 233–266 (2023).
86. Ortega, A., Amorós, D. & de la Torre, J. G. Prediction of hydrodynamic and other solution properties of rigid proteins from atomic- and residue-level models. *Biophys. J.* **101**, 892–898 (2011).
87. Johnson, K. A. & Borisy, G. G. Kinetic analysis of microtubule self-assembly in vitro. *J. Mol. Biol.* **117**, 1–31 (1977).
88. Punjani, A., Rubinstein, J. L., Fleet, D. J. & Brubaker, M. A. cryoSPARC: algorithms for rapid unsupervised cryo-EM structure determination. *Nat. Methods* **14**, 290–296 (2017).
89. Zheng, S. Q. et al. MotionCor2: anisotropic correction of beam-induced motion for improved cryo-electron microscopy. *Nat. Methods* **14**, 331–332 (2017).
90. Pettersen, E. F. et al. UCSF chimera—a visualization system for exploratory research and analysis. *J. Comput. Chem.* **25**, 1605–1612 (2004).
91. Adams, P. D. et al. PHENIX: a comprehensive Python-based system for macromolecular structure solution. *Acta Crystallogr. D* **66**, 213–221 (2010).
92. Emsley, P., Lohkamp, B., Scott, W. G. & Cowtan, K. Features and development of Coot. *Acta Crystallogr. D* **66**, 486–501 (2010).
93. Afonine, P. V. et al. Real-space refinement in PHENIX for cryo-EM and crystallography. *Acta Crystallogr. D* **74**, 531–544 (2018).
94. Chen, V. B. et al. MolProbity: all-atom structure validation for macromolecular crystallography. *Acta Crystallogr. D* **66**, 12–21 (2010).
95. Lashkov, A. A., Tolmachev, I. V., Eistrikh-Heller, P. A. & Rubinsky, S. V. PyFepRestr: plugin to PyMOL molecular graphics system for calculating the free energy of ligand–receptor binding. *Crystallogr. Rep.* **66**, 861–865 (2021).
96. Menegollo, M., Tessari, I., Bubacco, L. & Szabadkai, G. in *Calcium Signalling: Methods and Protocols* (eds Raffaello, A. & Vecellio Reane, D.) 223–232 (Springer, 2019).

Acknowledgements

We thank the members of the Tezcan group for extensive discussions and experimental assistance. We also thank M. Matyszewski of UCSD's cryo-EM facility and the members of S^2C^2 for help with data collection, data processing and computational support. This research was primarily supported by the US Department of Energy (DOE; Division of Materials Sciences, Biomolecular Materials; award DE-SC0003844 to F.A.T., for concept development, protein engineering and structural characterization). Additional support was provided by the National Science Foundation (NSF; Division of Materials Research; award DMR-2004558 to F.A.T., for biochemical assays) and by the DOE (as part of the Energy Frontier Research Centers program: the Center for the Science of Synthesis Across Scales under award number DE-SC0019288, for additional cryo-EM analysis). E.H.E. was supported by the National Institutes of Health (NIH; GM122510). The NIH also partially funds the UCSD EM Core (S10OD023527). S^2C^2 is supported by the NIH Common Fund transformative high-resolution cryo-EM program (U24 GM129541). The UCSD Materials Research Science and Engineering Center materials characterization facility is supported by the NSF (DMR-2011924).

Author contributions

Y.L. conceptualized the project, designed and performed all experiments, conducted the data analysis and cowrote the paper. J.Z. designed the biochemistry experiments and performed the TEM data collection. Z.Z. and Y.L. performed the cryo-EM data collection. Z.Z. and F.W. processed the cryo-EM data. J.W. and G.M. developed the kinetic models, performed the simulations and conducted the data analysis. T.P.J.K. oversaw the efforts on kinetics simulations. E.H.E. guided the cryo-EM data collection and analysis. F.A.T. initiated the project, guided the experiment design and data analysis and wrote the paper.

Competing interests

G.M. is an employee and T.P.J.K. is the founder of Wavebreak Therapeutics. The work reported here was not influenced by this connection. The other authors declare no competing interests.

Additional information

Supplementary information The online version contains supplementary material available at https://doi.org/10.1038/s41589-024-01811-1.

Correspondence and requests for materials should be addressed to F. Akif Tezcan.

Peer review information *Nature Chemical Biology* thanks Job Boekhoven, Rein Ulijn and the other, anonymous, reviewer(s) for their contribution to the peer review of this work.

nature portfolio

Corresponding author(s): F. Akif Tezcan

Last updated by author(s): Feb 14, 2024

Reporting Summary

Nature Portfolio wishes to improve the reproducibility of the work that we publish. This form provides structure for consistency and transparency in reporting. For further information on Nature Portfolio policies, see our Editorial Policies and the Editorial Policy Checklist.

Statistics

For all statistical analyses, confirm that the following items are present in the figure legend, table legend, main text, or Methods section.

n/a	Confirmed
☐	☒ The exact sample size (*n*) for each experimental group/condition, given as a discrete number and unit of measurement
☐	☒ A statement on whether measurements were taken from distinct samples or whether the same sample was measured repeatedly
☒	☐ The statistical test(s) used AND whether they are one- or two-sided *Only common tests should be described solely by name; describe more complex techniques in the Methods section.*
☒	☐ A description of all covariates tested
☒	☐ A description of any assumptions or corrections, such as tests of normality and adjustment for multiple comparisons
☐	☒ A full description of the statistical parameters including central tendency (e.g. means) or other basic estimates (e.g. regression coefficient) AND variation (e.g. standard deviation) or associated estimates of uncertainty (e.g. confidence intervals)
☒	☐ For null hypothesis testing, the test statistic (e.g. *F*, *t*, *r*) with confidence intervals, effect sizes, degrees of freedom and *P* value noted *Give P values as exact values whenever suitable.*
☒	☐ For Bayesian analysis, information on the choice of priors and Markov chain Monte Carlo settings
☒	☐ For hierarchical and complex designs, identification of the appropriate level for tests and full reporting of outcomes
☒	☐ Estimates of effect sizes (e.g. Cohen's *d*, Pearson's *r*), indicating how they were calculated

Our web collection on statistics for biologists contains articles on many of the points above.

Software and code

Policy information about availability of computer code

Data collection	Transmission Electron Microscope: DigitalMicrograph 3.5 Cryogenic Electron Microscopy: EPU 3.5 Dynamic Light Scattering: WyaG DynaPro NanoStar scattering: Tecan i-control UV/Vis: 8453 Agilent UV-Visible System AUC: Proteomelab Chromatography: Chromeleon 7 Electrospray ionization mass spectrometry: Xcalibur 4.3.73.11
Data analysis	Transmission Electron Microscope: Fiji Cryogenic Electron Microscopy: cryoSPARC (data process/reconstruction), UCSF Chimera and ChimeraX 1.7 (model fitting/molecular graphics), Phenix 1.14-3260 (model building/refinement), Coot v.0.8.9.2 (refinement) and The PyMOL Molecular Graphics System Version 2.4.0 (structure analysis/visualization) Scattering: Mathematica (simulation), AmyloFit (fitting) AUC: SEDFIT v16.1c Chromatography: Chromeleon 7 Electrospray ionization mass spectrometry: Xcalibur QualBrowser 4.3.73.11

For manuscripts utilizing custom algorithms or software that are central to the research but not yet described in published literature, software must be made available to editors and reviewers. We strongly encourage code deposition in a community repository (e.g. GitHub). See the Nature Portfolio guidelines for submitting code & software for further information.

Data

Policy information about availability of data

All manuscripts must include a data availability statement. This statement should provide the following information, where applicable:

- Accession codes, unique identifiers, or web links for publicly available datasets
- A description of any restrictions on data availability
- For clinical datasets or third party data, please ensure that the statement adheres to our policy

The principal data supporting the findings of this work are available within the figures and the Supplementary Information. The atomic coordinates and electron microscopy maps have been deposited in the Protein Data Bank (PDB) and Electron Microscopy Data Bank (EMDB) under accession codes: 8VW9/EMD-43577 (fresh ΔCFtsH nanotube-Group 1), 8VWA/EMD-43579 (fresh ΔCFtsH nanotube-Group 2), 8VWB/EMD-43580 (aged ΔCFtsH nanotube-Group 1), 8VWC/EMD-43581 (aged ΔCFtsH nanotube-Group 2). We utilized PDB ID 7TDO for initial model fitting.

Human research participants

Policy information about studies involving human research participants and Sex and Gender in Research.

Reporting on sex and gender	N/A
Population characteristics	N/A
Recruitment	N/A
Ethics oversight	N/A

Note that full information on the approval of the study protocol must also be provided in the manuscript.

Field-specific reporting

Please select the one below that is the best fit for your research. If you are not sure, read the appropriate sections before making your selection.

☒ Life sciences ☐ Behavioural & social sciences ☐ Ecological, evolutionary & environmental sciences

For a reference copy of the document with all sections, see nature.com/documents/nr-reporting-summary-flat.pdf

Life sciences study design

All studies must disclose on these points even when the disclosure is negative.

Sample size	Sample sizes were not calculated. The number of the replicates in all experiments was chosen based on the minimum amount required for statistical verification by standard deviation.
Data exclusions	No data was excluded from our study
Replication	Experiments were performed at least in duplicate to ensure reproducibility and statistical validity. Numerical data, presented as mean ± standard deviation (SD), were obtained through three biological replicates. Representative micrographs are shown from as least two independent experiments. All attempts at replication were successful. All raw data has been compiled and can be publicly reviewed under source data.
Randomization	Randomization was not relevant to our study because we did not include human subjects or animals.
Blinding	Blinding was not relevant to our study because we did not include human subjects or animals.

Reporting for specific materials, systems and methods

We require information from authors about some types of materials, experimental systems and methods used in many studies. Here, indicate whether each material, system or method listed is relevant to your study. If you are not sure if a list item applies to your research, read the appropriate section before selecting a response.

Materials & experimental systems

n/a	Involved in the study
☒	☐ Antibodies
☒	☐ Eukaryotic cell lines
☒	☐ Palaeontology and archaeology
☒	☐ Animals and other organisms
☒	☐ Clinical data
☒	☐ Dual use research of concern

Methods

n/a	Involved in the study
☒	☐ ChIP-seq
☒	☐ Flow cytometry
☒	☐ MRI-based neuroimaging